Astronomical Journal, in press (Jan 2001)

High-Redshift Quasars Found in Sloan Digital Sky Survey Commissioning Data III: A Color Selected Sample at $i^* < 20$ in the Fall Equatorial Stripe[1]

Xiaohui Fan[2,3], Michael A. Strauss[2], Gordon T. Richards[4,5], Jeffrey A. Newman[6], Robert H. Becker[7,8], Donald P. Schneider[5], James E. Gunn[2], Marc Davis[6], Richard L. White[9], Robert H. Lupton[2], John E. Anderson, Jr.[10], James Annis[10], Neta A. Bahcall[2], Robert J. Brunner[11], Istvan Csabai[13], Mamoru Doi[14], Masataka Fukugita[15,3], G. S. Hennessy[16], Robert B. Hindsley[17], Željko Ivezić[2], Gillian R. Knapp[2], Timothy A. McKay[18], Jeffrey A. Munn[19], Jeffrey R. Pier[19], Alexander S. Szalay[13], and Donald G. York[4]

ABSTRACT

This is the third paper in a series aimed at finding high-redshift quasars from five-color ($u'g'r'i'z'$) imaging data taken along the Celestial Equator by the Sloan Digital Sky Survey (SDSS) during its commissioning phase. In this paper, we first present the observations of 14 bright high-redshift quasars

---

[1]Based on observations obtained with the Sloan Digital Sky Survey, with the Apache Point Observatory 3.5-meter telescope, which is owned and operated by the Astrophysical Research Consortium, by the W. M. Keck Observatory, which is operated as a scientific partnership among the California Institute of Technology, the University of California, and NASA, and was made possible by the generous financial support of the W. M. Keck Foundation, and with the Hobby-Eberly Telescope, which is a joint project of the University of Texas at Austin, the Pennsylvania State University, Stanford University, Ludwig-Maximillians-Universität München, and Georg-August-Universität Göttingen.

[2]Princeton University Observatory, Princeton, NJ 08544

[3]Institute for Advanced Study, Olden Lane, Princeton, NJ 08540

[4]University of Chicago, Astronomy & Astrophysics Center, 5640 S. Ellis Ave., Chicago, IL 60637

[5]Department of Astronomy and Astrophysics, The Pennsylvania State University, University Park, PA 16802

[6]Department of Astronomy, University of California, Berkeley, CA 94720-3411

[7]Physics Dept., University of California, Davis, CA 95616

[8]IGPP/Lawrence Livermore National Laboratory

[9]Space Telescope Science Institute, Baltimore, MD 21218

[10]Fermi National Accelerator Laboratory, P.O. Box 500, Batavia, IL 60510

[11] Department of Astronomy, California Institute of Technology, Pasadena, CA 91125

[13] Department of Physics and Astronomy, The Johns Hopkins University, 3701 San Martin Drive, Baltimore, MD 21218, USA

[14]Department of Astronomy and Research Center for the Early Universe, School of Science, University of Tokyo, Hongo, Bunkyo, Tokyo, 113-0033 Japan

[15]Institute for Cosmic Ray Research, University of Tokyo, Midori, Tanashi, Tokyo 188-8502, Japan

[16]U.S. Naval Observatory, 3450 Massachusetts Ave., NW, Washington, DC 20392-5420

[17]Remote Sensing Division, Code 7215, Naval Research Laboratory, 4555 Overlook Ave. SW, Washington, DC 20375

[18]University of Michigan, Department of Physics, 500 East University, Ann Arbor, MI 48109

[19]U.S. Naval Observatory, Flagstaff Station, P.O. Box 1149, Flagstaff, AZ 86002-1149

($3.66 \leq z \leq 4.77$, $i^* \lesssim 20$) discovered in the SDSS Fall Equatorial Stripe, and the SDSS photometry of two previously known high-redshift quasars in the same region of the sky. Combined with the quasars presented in Fan et al. (1999) and Schneider et al. (2000b), we define a color-selected flux-limited sample of 39 quasars at $3.6 < z < 5.0$ and $i^* \lesssim 20$, covering a total effective area of 182 deg^2. From this sample, we estimate the average spectral power law slope in the rest-frame ultraviolet for quasars at $z \sim 4$ to be -0.79 with a standard deviation of 0.34, and the average rest-frame equivalent width of the Lyα+N V emission line to be 69 Å with a standard deviation of 18 Å.

The selection completeness of this multicolor sample is determined from the model colors of high-redshift quasars, taking into account the distributions of emission line strengths, intrinsic continuum slope, the line and continuum absorption from intervening material, and the effects of photometric errors. The average completeness of this sample is about 75%. The selection function calculated in this paper will be used to correct the incompleteness of this color-selected sample and to derive the high-redshift quasar luminosity function in a subsequent paper.

In the Appendix, we present the observations of an additional 18 faint quasars ($3.57 \leq z \leq 4.80$, $20.1 < i^* < 20.8$) discovered in the region on the sky that has been imaged twice. Several quasars presented in this paper exhibit interesting properties, including a radio-loud quasar at $z = 4.77$, and a narrow-line quasar (FWHM = 1500 km s^{-1}) at $z = 3.57$.

1. Introduction

This paper is the third in a series presenting high-redshift ($z > 3.6$) quasars selected from the commissioning data of the Sloan Digital Sky Survey (SDSS; York et al. 2000). In Papers I and II (Fan et al. 1999a, 2000a) in this series, and in Schneider et al. (2000a, b, 2001), we have presented the discovery of ~ 60 quasars at $z \gtrsim 3.6$, selected from ≈ 400 deg^2 of SDSS multicolor imaging data along the Celestial Equator. In this paper, we describe observations of additional quasar candidates selected in a similar manner in the Fall Equatorial Stripe, overlapping the areas covered by Fan et al. (1999a) and Schneider et al. (2000b), together defining a complete color-selected sample of bright high-redshift quasars covering 182 deg^2. In addition, we search for fainter high-redshift quasars based on areas of the sky that have been imaged twice by the SDSS.

In §2, we describe the photometric observations and quasar candidate selection. In

§3, we present the photometry and the spectroscopic observations of 14 newly discovered quasars in the Fall Equatorial Stripe at $z \gtrsim 3.6$ and $i^* \lesssim 20$, plus the observations of two previously known quasars in the same area of the sky. In this section, we also develop a method of using the measurements of emission line equivalent widths and broad-band multicolor photometry to estimate the slope of the intrinsic power-law continuum. In §4, we present the final flux-limited color-selected high-redshift quasar sample, which consists of 39 quasars at $i^* \lesssim 20$ and $3.6 < z < 5.0$ and covering 182 deg^2. The selection completeness of this sample is calculated in §5, based on a Monte-Carlo simulation of quasar colors as a function of redshift, using the quasar spectral model of Fan (1999). The effects of redshift, luminosity, continuum shape and emission line strength on the completeness of the survey are discussed in detail in §5. The results are summarized in §6. This color-selected sample is used to study the evolution of the quasar luminosity function at high redshift in a subsequent paper (Paper IV, Fan et al. 2000b).

In Appendix A, we provide updated information on the SDSS filter response functions, which are used to calculate quasar model colors and the selection function. Part of the Fall Equatorial Stripe area has been imaged multiple times during the commissioning phase, allowing a search for quasars fainter than $i^* \sim 20$. In Appendix B, we present the photometry and spectroscopy of 18 faint quasars discovered from these data. They do not yet form a complete sample with well-defined selection criteria.

2. Photometric Observations and Quasar Selection

The SDSS telescope (Siegmund et al. 2000), imaging camera (Gunn et al. 1998), and photometric data reduction (Lupton et al. 2000) are described in York et al. (2000) (see also Paper I). Briefly, the telescope, located at Apache Point Observatory in southeastern New Mexico, has a 2.5m primary mirror and a wide, essentially distortion-free field. The imaging camera contains thirty 2048×2048 photometric CCDs, which simultaneously observe 6 parallel $13'$ wide swaths, or *scanlines* of the sky, in 5 broad filters (u', g', r', i', and z') covering the entire optical band from the atmospheric cutoff in the blue to the silicon sensitivity cutoff in the red (Fukugita et al. 1996, see also Appendix A). The photometric data are taken in time-delay and integrate (TDI, or "drift-scan") mode at sidereal rate; a given point on the sky passes through each of the five filters in succession. The total integration time per filter is 54.1 seconds. The data were calibrated photometrically by observing secondary standards in the survey area using a 50cm telescope at Apache Point Observatory. The SDSS primary standard star network had not yet been finalized at the time of these observations, so the photometric calibration used in this paper is only accurate

to $\sim 10\%$, 2%, 2%, 2% and 7%, in the u', g', r', i', and z' bands, respectively. Thus as in Papers I and II, we will denote the preliminary SDSS magnitudes presented here as u^*, g^*, r^*, i^* and z^*, rather than the notation u', g', r', i' and z' that will be used for the final SDSS photometry, which will have photometric accuracy of $\lesssim 2\%$ for bright sources.

In this paper, we select bright ($i^* \lesssim 20$) high-redshift quasar candidates from two SDSS imaging runs (Run 94 and 125, see Table B1) in the Fall Equatorial Stripe at high Galactic latitude ($22^h20^m \lesssim \alpha_{2000} \lesssim 4^h30^m$). These two runs form a filled *stripe* 2.5 degrees wide in declination, centered on the Celestial Equator. Some quasars found from these two runs have already been presented in Paper I and in Schneider et al. (2000b). The photometric data reduction procedures are described in Paper I. In this paper, we use the photometric catalogs produced by the most recent version of the SDSS photometric pipeline, which now corrects for the time and spatial variation of the Point Spread Function (PSF) within a given $10' \times 13'$ CCD frame, improving both the photometric accuracy and the star-galaxy separation. The 5-σ limiting magnitudes are similar to those of Papers I and II, roughly 22.3, 22.6, 22.7, 22.4 and 20.5 in u^*, g^*, r^*, i^*, and z^*, respectively, for a single observation. The photometry from the new reduction has changed slightly from the those in Paper I, but the differences are almost always smaller than the quoted photometric errors. Figure 1 presents the color-color diagrams for all stellar sources at $i^* < 20.2$ in 25 deg^2 of the SDSS imaging data. The inner parts of the diagrams are shown as contours, linearly spaced in density of stars per unit area on the color-color diagram. As in Papers I and II, only sources that are detected in all three relevant bands at more than 5 σ are plotted. The median tracks of quasar colors as a function of redshift from Fan (1999) are also displayed in Figure 1.

High-redshift quasar candidates were selected using color cuts similar to those presented in Papers I and II. The final criteria we use to define the color-selected complete sample in §4 are based on the colors *after* correcting for Galactic extinction using the reddening map of Schlegel, Finkbeiner & Davis (1998). The criteria are as follows:

1. gri candidates, selected principally from the $g^* - r^*, r^* - i^*$ diagram:

$$\begin{aligned} &(a)\ i^* < 20.05 \\ &(b)\ u^* - g^* > 2.00 \text{ or } u^* > 21.00 \\ &(c)\ g^* - r^* > 1.00 \\ &(d)\ r^* - i^* < 0.42(g^* - r^*) - 0.31 \text{ or } g^* - r^* > 2.30 \\ &(e)\ i^* - z^* < 0.25 \end{aligned} \tag{1}$$

2. riz candidates, selected principally from the $r^* - i^*, i^* - z^*$ diagram:

$$
\begin{aligned}
&(a)\ i^* < 20.20 \\
&(b)\ u^* > 22.00 \\
&(c)\ g^* > 22.60 \\
&(d)\ r^* - i^* > 1.00 \\
&(e)\ i^* - z^* < 0.47(r^* - i^*) - 0.48
\end{aligned}
\tag{2}
$$

The intersections of those color cuts with the $g^* - r^*, r^* - i^*$ and $r^* - i^*, i^* - z^*$ diagrams are illustrated in Figure 1. The final criteria are more restrictive than those used in Papers I and II, in the sense that the cuts are further away from the stellar locus. Because of the limited observing time for spectroscopic follow-up observations, we used this tighter cut to limit the number of contaminants among the candidates in order to complete the sample in the Fall 1999 observing season. This modification increases the observing efficiency at the cost of lower selection completeness. The completeness function of the color selection criteria, and the effects of different selection constraints on the sample are presented in §5. In the SDSS main spectroscopic survey, the quasar candidates are selected in multi-dimensional color space using a more complicated algorithm (Newberg et al. 2000, in preparation, see also Newberg & Yanny 1997).

Paper I presented the photometry of two previously known quasars from Run 94 data. In Run 125 (in an area not covered by Paper I), two additional quasars are recovered. SDSSp J005922.65+000301.4[19] is reported in Kennefick, Djorgovski & de Carvalho (1995) as PSS 0059+0003 ($z = 4.16$). No information on the other quasar, SDSSp J024457.19–010809.9, has been published in the literature, but it is reported at the DPOSS website[20] as PSS 0244–0108. We obtained its spectrum in order to measure its spectral properties.

3. Spectroscopic Observations

Thirty-three quasar candidates that meet the criteria described in §2 were observed in the Fall 1999 observing season using the Keck II telescope and the Hobby-Eberly Telescope (HET). Twenty-five of the candidates are identified as high-redshift quasars at $z > 3.6$. The HET observations of 11 new quasars are presented in a separate paper (Schneider et al. 2000b). Here we present the Keck observations.

---

[19]The naming convention for the SDSS sources is SDSSp JHHMMSS.SS±DDMMSS.S, where "p" stands for the preliminary SDSS astrometry, and the positions are expressed in J2000.0 coordinates. The astrometry is accurate to better than $0.2''$ in each axis.

[20]`http://astro.caltech.edu/~george/z4.qso`

Spectra of 12 SDSS high-redshift quasars were taken with the Keck II telescope, using the Low Resolution Imaging Spectrograph (LRIS, Oke et al. 1995) on the nights of 1999 October 15 and 16. A 300 line mm^{-1} grating was used. Two quasars (SDSSp J012700.69−004559.1 and SDSSp J021043.17−001818.4) were observed with Keck II/LRIS on 1999 July 21, when a 400 line mm^{-1} grating was used. The exposure times ranged from 600 s to 1200 s. Observations of the spectrophotometric standard Feige 110 (Massey 1988, Massey & Gronwall 1990) were used to provide flux calibrations and to correct for telluric absorption, and observations of Hg-Ne-Ar lamps were used for wavelength calibration. The spectra were reduced with standard IRAF procedures. The calibrated spectra extend from 4000 Å to 9000 Å for the 300 line mm^{-1} grating spectra, with a dispersion of 2.4 Å/pixel. Note that at 8000 Å$< \lambda <$ 9000 Å, the spectrum is slightly affected by second-order contamination from $4000 < \lambda <$ 4500 Å. However, there is little flux at at $\lambda <$ 4500Å for high-redshift quasars due to the absorption systems, and we did not notice any order-overlap effect in the data. The second-order effect, however, does somewhat affect the standard star observation, the flux calibration, and the removal of the telluric bands. The spectral coverage is 4000 Å to 8000 Å for the 400 line mm^{-1} grating spectra, with a dispersion of 1.9 Å/pixel. The resolution of the LRIS spectra is $\sim$ 7 Å. In addition, spectra of SDSSp J024457.19–010809.9 (PSS 0244–0108) were obtained with the ARC 3.5m telescope using the Double Imaging Spectrograph (DIS) on the night of 1999 December 28 for a total exposure time of 2400 s. The DIS instrument and spectral data reduction procedures were described in Paper I.

Table 1 gives the positions, SDSS photometry and redshifts of the 14 new SDSS high-redshift quasars, and the photometric run from which they were selected, as well as the SDSS measurements of the two previously-known quasars. The photometry is expressed in asinh magnitudes (Lupton, Gunn & Szalay 1999, see also Paper I). The photometric errors given are only statistical, and do not include calibration errors. Note that all but one objects presented in this paper are selected from Run 125. Most of the candidates from Run 94 are presented in Paper I and in Schneider et al. (2000b). Positions of the 16 confirmed SDSS quasars presented in this paper are plotted on the color-color diagrams (Figure 1a and 1c) as filled circles. Positions of other quasars in the same survey area and non-quasars that satisfied the selection criteria are also shown in Figure 1. Finding charts of all objects in Table 1 are given in Figure 2. They are $160'' \times 160''$ i' band SDSS images with an effective exposure time of 54.1 seconds.

We matched the positions of quasars in Table 2 against the FIRST radio survey (Becker, White, & Helfand 1995). Three of them have FIRST counterparts at 20 cm at the 1 mJy level (with positional matches better than 1″): SDSSp J013108.19+005248.2 ($z = 4.19$), SDSSp J021043.17–001818.4 ($z = 4.77$) and SDSSp J030025.23+003224.2

($z = 4.19$), correspond to unresolved FIRST sources of 4.00, 9.75 and 7.56 mJy at 20 cm, respectively. In particular, SDSSp J021043.17–001818.4 ($z = 4.77$) is the highest redshift radio-loud luminous quasar yet known. None of the objects was detected in the ROSAT full-sky pixel images (Voges et al. 1999) at a typical 3σ upper limit of 3×10^{-13} erg s^{-1} cm^{-2} in the 0.1 – 2.4 keV band.

Figure 3 presents the spectra of the 14 newly discovered SDSS quasars and of SDSSp J024457.19–010809.9 (PSS 0244–0108). In the figure, we place the spectra on an absolute flux scale (to compensate for the uncertainties due to non-photometric conditions and variable seeing during the night) by forcing the synthetic i^* magnitudes from the spectra to be the same as the SDSS photometric measurements. The emission line properties of the quasars are listed in Table 2. Central wavelengths and rest frame equivalent widths of five major emission lines are measured following the procedures of Paper I.

3.1. Determination of Continuum Properties

We assume the quasar continuum is a power law with a slope α: $f_\nu \propto \nu^\alpha$ (or $f_\lambda \propto \lambda^{-\alpha-2}$). The continuum magnitude, AB_{1450}, is defined as the AB magnitude at $\lambda = 1450$ Å in the rest frame corrected for Galactic extinction. AB magnitude can be converted to flux units as:

$$AB_\nu = -2.5 \log f_\nu - 48.60, \tag{3}$$

where f_ν has units of erg s^{-1} cm^{-2} Hz^{-1}. For a power law continuum, AB_{1450} can be converted to the rest-frame Kron-Cousins B band magnitude:

$$B = AB_{1450} + 2.5\alpha \log(4400/1450) + 0.12. \tag{4}$$

The effective wavelength in the B band is 4400 Å, and the factor 0.12 is the zeropoint difference between the AB magnitude system and the Vega-based system in the B band (Schmidt, Schneider & Gunn 1995).

Table 3 gives the continuum properties of the quasars. As in Paper I, redshifts are determined from all emission lines redward of Lyα; Lyα itself is not used, due to absorption from the Lyα forest on its blue side. The parameters α and AB_{1450} can be determined from the spectrum alone. However, not all our observations were carried out under photometric conditions or with the slit at the parallactic angle. The observed continuum range redward of the Lyα emission covered by the spectra ($1216(1+z)$ Å to 9000 Å) of these high-redshift quasars is typically only few hundred Å in the rest frame. Moreover, some of the spectra have rather poor signal-to-noise ratio beyond 8000 Å. Thus, in some cases, it is difficult to determine accurately the continuum slope α from the observed spectrum.

However, the broad-band photometry gives us an alternative method to determine the slope. The intrinsic quasar spectrum can be modeled as a power-law continuum plus a series of emission lines. The equivalent width of the lines can be measured quite accurately from the spectrum. Therefore, the slope of the power-law can be determined by matching the spectral model to the broad-band photometry. The SDSS z' cutoff is beyond 10,000 Å, so this gives a broader baseline over which to determine the slope. Moreover, the absolute photometric calibration is more accurate. The contribution to the broad-band colors from emission lines other than Lyα is also small. However, only bands which are not affected by Lyα forest lines can be used in this method. At $z > 4.5$, Lyα moves into the i' band, making it impossible to determine the slope from the z' measurement alone. Therefore, we develop a method to fit the continuum slope α and to derive AB_{1450} of the quasar using information from both the observed spectrum and the broad-band photometry. Briefly, we construct a quasar spectral model that uses the observed spectrum blueward of Lyα emission and the power-law continuum plus emission line model redward of Lyα emission, and determine α and AB_{1450} by finding the model that fits the photometry the best. In detail, the method consists of following steps:

(1) Obtain a corrected observed spectrum f_λ^{obs} that matches the SDSS photometry. For quasars with $i^* < 20$ and $z < 4.3$, the photometric errors in the r' and i' bands are small (< 0.04 mag). We apply an additional correction function linear in wavelength (with two free parameters, a zeropoint and a slope) to the spectrum so that the synthetic photometry reproduces the SDSS r^* and i^* magnitudes. For objects at $z > 4.3$, the Lyα forest moves into r', increasing the error in the r' band, therefore we only apply a zeropoint shift to match the i^* magnitude.

(2) For a given α and AB_{1450}, construct a model spectrum f_λ^{model}:

$$f_\lambda^{model} = \begin{cases} f_\lambda^{obs} & \text{if } \lambda < 1260 \text{ Å}\times(1+z), \\ f_{1450}[\lambda/1450(1+z)]^{-\alpha-2} \cdot \sum_i [1 + \mathrm{EW}_i P(\lambda - \lambda_0^i)] & \text{if } \lambda > 1260 \text{ Å}\times(1+z). \end{cases} \quad (5)$$

For $\lambda < 1260 \times (1+z)$, we use the flux from the corrected observed spectrum f_λ^{obs}. The observed profile for the Lyα+N V emission line is used as the line is strongly affected by the Lyα forest absorption. For $\lambda > 1260 \times (1+z)$, the model spectrum has three components:

(a) a power law continuum with $f_\lambda \propto \lambda^{-\alpha-2}$ and continuum magnitude AB_{1450};

(b) emission lines. We use the equivalent widths measured in Table 2 for strong lines. For weak lines, we use the line ratios in Francis et al. (1991) to scale from the measured Lyα+N V emission line strength. The line profile $P(\lambda)$ is assumed to be a Gaussian with FWHM of 5000 km s^{-1}. The choice of FWHM has negligible effect on the broad-band

colors;

(c) if there is any broad absorption or strong associated absorption system in the spectrum, the equivalent widths and FWHMs are measured and the lines are added to the spectrum.

(3) Obtain the best fit α and AB_{1450}. First, for a given (α, AB_{1450}), the synthetic SDSS magnitudes m^{model} are calculated from the model spectrum. We add the statistical error in Table 1 and the calibration error (§2) of the SDSS photometry in quadrature to obtain the final photometric error σ_i^{obs}. Then we minimize the total χ^2 of the differences between the synthetic magnitudes and the SDSS photometry m^{obs} with respect to α and AB_{1450}:

$$\chi^2 = \sum_i \left(\frac{m_i^{model} - m_i^{obs}}{\sigma_i^{obs}} \right)^2 . \quad (6)$$

For quasars at $z < 4.3$, $\lambda = 1260 \times (1 + z)$ is still inside the SDSS r' band, while the u' and g' bands are dominated by the absorption systems. Therefore, r^*, i^* and z^* magnitudes are used. For quasars at $z > 4.3$, only i^* and z^* magnitudes can provide useful constraints on the continuum slope, and only these bands are used in the fit. The 1-σ errors on the parameters are estimated by finding the values that give $\chi^2 = \chi^2_{min} + 1$, where χ^2_{min} is for the best-fit parameters. The error on α is ~ 0.20 for $z < 4.3$ and ~ 0.5 for $z > 4.3$, and the error on AB_{1450} is typically a few percent. The best-fit values and 1-σ errors of α and AB_{1450} are given in Table 3. An example of the result of this fitting procedure is shown in Figure 4.

The major reason for determining α in this paper is to estimate the selection completeness of the survey, as the selection probability varies with different continuum shape (and therefore different broad-band colors). For objects with high signal-to-noise ratio spectra, the α values determined from the spectra and from the method above are usually consistent with each other within the quoted error. Determining α using broad-band photometry does not depend on the selection of a continuum window, and the error bar is easy to interpret. The best-fit α using the method above always minimizes the difference between model and observed colors. By tying to the observed colors rather than fitting the observed spectra, the effect of photometric calibration errors (at 2% – 7% level in this paper) on the selection completeness calculation is minimized: an error on the photometric calibration or uncertainties in the filter response would give rise to a wrong best-fit α, but to first order, the spectral model in §5 based on these α values should still reproduce the observed color distribution.

For the survey selection function (§5) and the quasar luminosity function (Paper IV), the calculations are carried out in two cosmologies: a model with $\Omega_m = 1$ and $H_0 = 50$ km

s^{-1} km^{-1}, where we refer to as the $\Omega = 1$ model hereafter; and a Λ-dominated flat model with $\Omega_m = 0.35$, $\Lambda = 0.65$ and $H_0 = 65$ km s^{-1} km^{-1}, which we refer to as the Λ-model hereafter. In this paper, most of the results are presented using the $\Omega = 1$ model. Table 3 gives the absolute magnitude at 1450 Å in the rest frame, M_{1450}, for the $\Omega = 1$ model. In Paper IV, we use the M_{1450} values to derive the quasar luminosity function, and compare with low-redshift results after converting to the rest-frame B-band. All the continuum properties of Table 3 have been corrected for Galactic extinction using the reddening map of Schlegel, Finkbeiner & Davis (1998) assuming a standard extinction curve.

3.2. Notes on Individual Objects

SDSSp J012700.69–004559.1 ($z = 4.06$). A prominent damped Lyα absorption line candidate is detected at $\lambda = 5742$ Å ($z_{abs} = 3.72$), with a rest-frame equivalent width of 33 Å. The corresponding metal line systems (the C IV doublet at 7330/7317 Å, and the Si IV doublet at 6632/6589 Å) are also detected.

SDSSp J021043.17–001818.4 ($z = 4.77$). This is the highest redshift radio loud quasar known to date, and is located only 10.4′ away from SDSSp J021102.72–000910.3 ($z = 4.90$). The co-moving separation of the two quasars is 29.7 h^{-1} Mpc for $\Omega = 1$.

SDSSp J024457.19–010809.9 ($z = 3.96$). This is the previously-known quasar PSS 0244–0108, which has a reported redshift of $z = 4.01$ on the DPOSS website [21]. It is a BAL quasar. Strong BAL troughs due to Lyα+N V and C IV are clearly visible in the spectrum. The C IV BAL trough has a velocity of ~ 17200 km s^{-1} and FWHM of ~ 8600 km s^{-1}. The redshift determination is not straightforward for BAL quasars due to the presence of strong absorption features. The redshift reported here is the average of redshifts from the peaks of the O I and Si IV emission lines.

SDSSp J025019.78+004650.3 ($z = 4.76$). Typically, quasars at $z > 4.5$ would encounter a Lyman Limit System within 0.1 of its emission line redshift (Schneider, Schmidt & Gunn 1991, Paper I). A strong Lyman Limit System (LLS) in this quasar is detected only at $z = 4.24$ ($\lambda \sim 4780$ Å). As a result, this object is detected at the 5-σ level in the g' band. If we assume the number density of the LLS $N(z) = 0.27(1+z)^{1.55}$ (Storrie-Lombardi & Irwin 1994), the fraction of quasars at $z = 4.76$ without a LLS at $z > 4.24$ is 13%.

SDSSp J030707.46–001601.4 ($z = 3.70$). A metal absorption system at $z = 3.64$ is detected based on the C IV doublet at 7200/7186 Å and the Si IV doublet at 6514/6471 Å.

[21] `http://astro.caltech.edu/~george/z4.qso`

A Mg II system at $z = 1.29$ is also detected (the doublet at 6430/6414 Å).

4. The Fall Equatorial Stripe Sample

Using the selection criteria presented in §2 (Eq. 1 and 2), we define a complete color-selected high-redshift quasar sample in the Fall Equatorial Stripe. This complete sample covers the area of SDSS Runs 94 and 125. The right ascension of Run 94 ranges from 22^h22^m to 3^h55^m. For Run 125, we only include areas with $23^h18^m < \alpha_{2000} < 4^h$, because the reddening increases to $E(B-V) > 0.2$ and becomes patchy at $\alpha_{2000} > 4^h$ at the east end of Run 125. After further correcting for (a) the overlap between Run 94 and 125 ($\sim 7\%$), (b) small areas of the sky with very poor seeing, and (c) areas on the CCDs affected by bright stars and defects which do not allow accurate measurements of the colors, the total effective area of the sample is 181.9 deg^2. During the selection process, we also rejected objects with flags indicating problems with image processing, in most cases associated with deblending of close neighbors (see Lupton 2000), and some objects are further rejected upon visual inspection of the image. The area covered by such objects is negligible.

The final color-selected sample contains 39 quasars at $3.6 < z < 5.0$. It includes 14 quasars presented in Paper I, 11 quasars presented in Schneider et al. (2000b) and 14 quasars presented in this paper. Figure 1 shows the positions of all the quasars presented in these three papers on the color-color diagrams. Several quasars in the same area of the sky in these papers are not part of the sample because they do not satisfy the final color selection criteria, either due to the tighter selection compared to the criteria in Paper I, or due to slight changes in the photometric zeropoints in the new photometric catalog.

In Figures 1(b) and (d), we plot the positions of the 14 non-quasars in the survey area that satisfy the selection criteria in the color-color diagrams. Among them, seven are galaxies with redshifts between 0.37 and 0.74. They all have compact morphology and are classified as stellar sources in the photometric catalog. With the exception of one with poor signal-to-noise ratio, all are identified as E+A (or k+A) galaxies showing strong Balmer break, Balmer absorption lines and weak emission lines (Dressler & Gunn 1982, Poggianti et al. 1999). Their broad-band colors are similar to those of high-redshift quasars: the strong Balmer break mimics the Lyman break in the quasar spectrum, while the continuum of E+A galaxies redward of the Balmer break is also blue, due to the contributions of the A–F stars in the galaxy. Five of the non-quasars are stars: one is a faint Carbon star (Margon et al. 2000, in preparation), while the other four seem to be normal stars scattered out of the stellar locus by photometric errors. We are not able to classify the other two objects.

One has very poor signal-to-noise ratio; we will discuss the nature of the other unclassified object in a separate paper (Fan et al. 2000 in preparation). Among the 53 objects that satisfy the final selection criteria, 39 are quasars, giving a success rate of 73%. This is higher than the 63% success rate quoted in Paper I. Several of non-quasars in Paper I no longer satisfy the tighter final selection with improved photometry. Note that most of the non-quasars are very close to the selection boundary.

In Table 4, we present the properties of the 39 quasars. The continuum magnitude and the continuum slope are calculated following the procedures described in §3.1. For quasars in Paper I, these quantities are re-measured based on improved (although not final) SDSS photometry. For the three previously known quasars for which we did not obtain new spectra, we use the spectral properties measured in Smith et al. (1994) and Kennefick, Djorgovski & de Carvalho (1995) and the SDSS photometry to derive their continuum magnitudes and power-law slopes. Table 4 also lists the detection probability of each quasar, which is described in the next section.

The sample in Table 4 covers a redshift range of $3.66 \leq z \leq 5.00$, and an absolute magnitude range of $-25.69 \leq M_{1450} \leq -27.72$ for the $\Omega = 1$ model. This is the largest complete sample of quasars at $z > 3.6$ to date. It includes 18 quasars at $z > 4.0$ and six at $z > 4.5$, enabling us to determine the quasar number density at $z \sim 4.8$ (Paper IV). By comparison, the Schmidt, Schneider & Gunn (1995) sample has 9 quasars at $z > 4.0$ with one at $z > 4.5$, and the Kennefick, Djorgovski & de Carvalho (1995) sample includes 10 quasars at $z > 4.0$ with a highest redshift of 4.45.

About 10% of optically selected low-redshift quasars are BALs (Weymann et al. 1991). In this sample, two of the quasars (SDSSp J023909.98–002121.5 and SDSSp J024457.19–010809.9) are classical BAL quasars; two other quasars (SDSSp 015048.83+004126.2 and SDSSp 033910.53–003009.2) are candidate mini-BAL quasars. The result is consistent with the fraction found in low-redshift samples. However, some of the spectra have poor signal-to-noise ratio, and we have not yet applied an objective criteria for selecting BALs to all the spectra, so this fraction is likely to be a lower limit. At least one object, SDSSp J033829.31+002156.3 ($z = 5.00$), also shows a strong and broad CIV absorption feature in a high signal-to-noise ratio spectrum (Songaila et al. 1999).

Schmidt et al. (1995) and Stern et al. (2000) found that about 10% of known quasars at $z > 4$ (most of which are also color-selected) are detected at radio wavelengths at the mJy level. Four quasars in our sample are FIRST radio sources with total flux of 4.0 – 9.8 mJy at 20cm. Although our sample size is still small, the fraction of radio-loud quasars in our sample is consistent with the previous results.

5. The Selection Function of the Color-Selected Sample

To derive the luminosity function of high-redshift quasars from the color-selected sample in Table 4, we first need to calculate the selection function. It is defined as the probability, $p(M_{1450}, z, SED)$, that a quasar of a given M_{1450}, z, and spectral energy distribution (SED) will satisfy the color selection criteria (Eqs. 1 and 2), In this section, we calculate the selection function using a Monte-Carlo simulation of quasar colors, based on the quasar spectral model described in Fan (1999). Similar procedures were adopted to calculate the selection function for multicolor quasar surveys by Warren, Hewett & Osmer (1994) and Kennefick, Djorgovski & de Carvalho (1995).

The measured colors of a quasar at a certain redshift and luminosity are determined by three factors: its intrinsic SED; the absorption systems that are distributed randomly along the line of sight; and the photometric errors. In §5.1, we describe the quasar spectral model and calculate the detection probability $p(M_{1450}, z, SED)$ of individual quasars, taking into account the effects of the distribution of absorption systems and photometric errors. We discuss in detail how this probability varies with different parameters, and how the selection criteria affect the sample completeness. In §5.2, we calculate the distribution of the intrinsic properties of quasars, the continuum slopes α and equivalent widths of Lyα+N V emission, based on the sample in Table 4, after correcting for the detection probability calculated in §5.1. Finally, in §5.3, we calculate the average selection probability of the quasar sample as a function of redshift and luminosity.

5.1. Detection Probability of Individual Quasars

To determine the detection probability, we first calculate the synthetic distribution of quasar colors at a given (M_{1450}, z, SED), following the procedures described in Fan (1999). As in that paper and in §3.1, the intrinsic quasar spectrum model, including a power law continuum and a series of emission lines, is parameterized by the continuum slope α and the rest-frame equivalent width of the Lyα+NV emission line, EW(Lyα+NV) (abbreviated to EW in what follows). The synthetic absorption spectrum takes into account intervening HI absorbers along the line of sight, including Lyα forest systems, Lyman Limit Systems and damped Lyman α systems. We use the distribution functions of each kind of absorber used by Fan (1999).

We calculate the SDSS magnitudes from the model spectrum and add photometric errors in each band. Our precedures differ in two ways from those of Appendix A of Fan (1999). First, we use updated SDSS filter response functions as described in Appendix

A. They are slightly different from those of Fukugita et al. (1996); in particular, the long-wavelength cutoff of the g', r', i' and z' filters are 100 – 300 Å bluer in the new measurements than in the old ones. For these broad-band filters, this difference has only a small effect on the colors of normal stars. However, it does affect the model quasar colors in certain redshift ranges for which the strong Lyα emission line is near a filter edge. Second, in the current calculation, we use the measured seeing for Runs 94 and 125, $\sim 1.6''$, to derive the photon noise of the PSF photometry. The seeing in these commissioning runs is worse than the $1.1''$ seeing assumed in Fan (1999). We further add the systematic calibration error in each band in quadrature to the random errors, as in §3.1.

For each object in the complete sample, a total of 1000 model quasars with the same $(M_{1450}, z, \alpha, EW)$ are generated, and SDSS magnitudes calculated. The fraction of these which satisfy the selection criteria of Eqs. (1) and (2) is defined to be the detection probability p, as listed in Table 4. It ranges from $\sim 100\%$ for objects located in the part of the color-color diagrams farthest away from the stellar locus (see Figure 1) to $\sim 40\%$ for the objects near the boundary of the selection criteria. An object with a given intrinsic spectrum can move in and out of the selected region in color space due to differing amounts of absorption and photometric errors. The average probability $\langle p \rangle = 0.80$ for the whole sample. This is considerably higher than that of Warren et al. (1994), $\langle p \rangle \sim 0.5$; the higher photometric accuracy with CCDs enables us to probe much closer to the stellar locus in color space than do surveys using photographic plate data.

Note that the spectral model above does not include contributions from BALs. For the four possible BAL quasars in our sample, we also calculate the detection probability by adding the observed BAL troughs in the model spectra. The detection probability changed by $\lesssim 10\%$ in all four cases. There is no systematic effect and $\langle p \rangle$ remains at 0.78 for the whole sample.

The color-selection criteria in Eqs. (1) and (2) choose regions in color space well-separated from the stellar locus. Quasars with redder continua (larger $|\alpha|$) and weaker emission lines are located in regions in the color-color diagrams close to normal stars. Any color-based selection will naturally select against these quasars. There may exist quasars with an intrinsic SED shape such that their broad-band colors are so similar to normal stars that their detection probability is close to zero. Thus it is difficult to correctly estimate the fraction of quasars that we would never find without assuming an *a priori* model for the intrinsic distribution of α and EW. The selection probability is also a strong function of the redshift and luminosity of the quasar. In Figure 5, we present the detection probability as a function of α and EW at several different redshifts and luminosities to illustrate the dependence of p on these parameters.

Figure 5(a) shows p at $z = 3.7$ and $M_{1450} = -27$ ($\Omega = 1$ model); this is near the lower redshift cutoff of the survey. The quasar is much brighter than the flux limit, so photometric errors are not important. In this case, a quasar with $\alpha \sim -0.8$ and EW = 70 Å, which are the mean values we derive in §5.2, has $p \sim 80\%$; the completeness is rather high. The completeness is lower for objects with redder continua or weaker emission lines. The detectability drops to $\sim 20\%$ at $\alpha \sim -1.6$, where $i - z \gtrsim 0.25$. This selection bias is introduced by the selection criterion $i^* - z^* < 0.25$. This eliminates a large number of compact E+A galaxies at $z \sim 0.4$ which have very similar $g^* - r^*$ and $r^* - i^*$ colors to $z \sim 4$ quasars but are intrinsically redder than are quasars. In the final selection of the SDSS main quasar sample, this condition will be relaxed. For objects with weak emission lines, p drops for bluer continua as well. At $z \sim 3.7$, such objects could have $g^* - r^* < 1.0$, and are thus excluded by the cut Eq. 1(c). This bias only affects redshifts close to the cutoff.

Figure 5(b) shows p at $z = 3.7$ and $M_{1450} = -25.5$, corresponding to $m_{1450} \sim 20$. This figure is for the same redshift as Figure 5(a), but at the survey limiting luminosity. In this case, p is much lower. At a given absolute magnitude, the *observed* apparent magnitudes of a substantial fraction of quasars will be below the apparent magnitude cut ($i^* < 20.05$) due to photometric errors. In addition, the large error in the g' band will scatter more quasars out of the selected region. However, the selection is actually somewhat more sensitive to larger α here than for brighter objects at the same redshift (Figure 5a): $p \sim 20\%$ for $\alpha \sim -1.8$. This is because the photometric error in z' is ~ 0.15 mag, scattering some objects with red intrinsic continua back into the sample with $i^* - z^* \lesssim 0.25$.

At $z \sim 4.5$, the Lyα emission has moved out of the SDSS r' band, and lies in the gap between r' and i'. Thus neither the gri nor the riz selection are sensitive to these quasars. Figure 5(c) shows the detection probability at this redshift and at $M_{1450} = -26.0$, near the survey limiting luminosity. This is the region where the survey is most incomplete. For typical values of α and emission line strength, $p \sim 50\%$. At most redshifts, the presence of a strong Lyα emission line makes the Lyman break in the spectrum more distinct, pushing the object further away from the stellar locus in color space. At $z \sim 4.5$, however, with the Lyα emission line in the gap, quasars are closer to the stellar locus than either at higher or lower redshift, making them difficult to select.

At $4.6 < z < 5.2$ (see Figure 1), the presence of strong Lyα forest absorption in the spectrum causes the object to be very well separated from the stellar locus in the $r^* - i^*$ vs. $i^* - z^*$ color-color diagram. Figure 5(d) shows that at $z = 5.0$, the selection completeness is very high, even for objects with weak emission lines or red continua. SDSS 1532–00 (Fan et al. 1999b), a $z = 4.62$ quasar without emission lines, was found in the SDSS Spring Equatorial Stripe data using with the same selection criteria. This demonstrates that our

selection is not sensitive to emission line strength in this redshift range.

Thus, except in the redshift range $z \sim 4.4 - 4.5$ and for luminosities near the survey limit, the detection probability is high and the selection criteria are sensitive to a large range of (α, EW). We will further examine the average selection function in §5.3 after deriving the distribution functions of the continuum slope and emission line strength in our sample.

5.2. Distribution of Equivalent Width and Continuum Slope

In this subsection, we use the sample in Table 4 to estimate the distributions of α and EW(Lyα+NV), after correcting the selection probability of each quasar. We first calculate their weighted means, then derive their distribution functions using a maximum likelihood approach and assume Gaussian distributions. The histograms in Figure 6 show the observed distributions of the power-law continuum slope, α, and the rest-frame equivalent width of Lyα+NV emission, EW. Using only the 35 non-BAL quasars, and weighting each object by the inverse of its selection probability $\frac{1}{p_i}$ (Table 4), we find a mean EW of 71.0 Å with a standard deviation of 18.3 Å, at an average redshift $\langle z \rangle = 4.06$. Similarly, using all 39 quasars in the sample, and applying a weight of $\frac{1}{p_i \delta_i^2(\alpha)}$, where $\delta_i(\alpha)$ is the error on the α measurement, we find a mean α of -0.80 with a standard deviation of 0.40.

However, these distributions can be biased if there is a population of quasars with small p which are totally missing from the sample. Thus, we use a maximum likelihood approach. The likelihood of the observed $(\alpha_i, \mathrm{EW}_i)$ is given by:

$$L = \prod_i \frac{p_i f(\alpha_i) f(\mathrm{EW}_i)}{\int p(\alpha, \mathrm{EW}) f(\alpha) f(\mathrm{EW}) d\alpha \; d(\mathrm{EW})} \tag{7}$$

where $f(\alpha)$ and $f(\mathrm{EW})$ are the distribution functions of α and EW. We assume both to be Gaussian, and uncorrelated with each other,

$$f(\alpha_i) = \frac{1}{2\pi\sqrt{\delta_i^2 + \sigma_\alpha^2}} \exp\left[-\frac{(\alpha_i - \overline{\alpha})^2}{2(\delta_i^2 + \sigma_\alpha^2)}\right]. \tag{8}$$

where $\overline{\alpha}$ and σ_α are the mean and standard deviation of its intrinsic distribution. Similarly,

$$f(\mathrm{EW}) = \frac{1}{2\pi\sigma_{\mathrm{EW}}} \exp\left[-\frac{(\mathrm{EW}_i - \overline{\mathrm{EW}})^2}{2\sigma_{\mathrm{EW}}^2}\right]. \tag{9}$$

Note that the normalizing integral $\int p(\alpha, \mathrm{EW}) f(\alpha) f(\mathrm{EW}) d\alpha \; d\mathrm{EW}$ in the denominator of the likelihood function is essential; without it, the maximum likelihood solution would

not depend on the choice of p, which is clearly wrong. However, as we show in §5.1, the selection function p is a complicated function of M_{1450}, z, α and EW. This integral cannot be evaluated without knowing the underlying distribution function of z and M_{1450}, namely, the luminosity function. A full solution requires maximizing the likelihood of the full distribution function $p(M_{1450}, z, \alpha, \mathrm{EW}) f(M_{1450}, z, \alpha, \mathrm{EW})$. We will present the maximum likelihood solution of the luminosity function in Paper IV, but we find that the distributions of α and EW are rather insensitive to the choice of luminosity function, as it provides a weighting of the probability function, which is only a slow varying function of z and M_{1450}. Using the luminosity function we find in Paper IV (for the $\Omega = 1$ model),

$$\log \Phi(M_{1450}, z) = -7.24 - 0.48(z - 3) + 0.63(M_{1450} + 26), \tag{10}$$

where $\Phi(M_{1450}, z)$ is the cumulative luminosity function in units of comoving Mpc^{-3}, we find: $\langle \mathrm{EW} \rangle = 69.3$ Å, $\sigma_{\mathrm{EW}} = 18.0$ Å, $\langle \alpha \rangle = -0.79$, and $\sigma_\alpha = 0.34$. In Figure 6, the average α value from the maximum likelihood solution is clearly offset from the *observed* distribution, due to the selection bias against objects with redder continua. The results above assume that the distributions of α and EW are not correlated with each other or with redshift or luminosity. Luminosity and emission line strength are known to be correlated (the Baldwin (1977) effect), although for the small luminosity range (2 mag) our sample covers, this is a rather small effect. These results change by less than 5% for a change of the parameters in the assumed luminosity function by $\sim 30\%$.

These statistics can be compared with results from previous studies. Based on 30 quasars at $3.1 < z < 4.75$, Schneider et al. (1991) found $\mathrm{EW(Ly}\alpha + \mathrm{NV}) = 82.3 \pm 29.8$ Å. Note that most of the quasars in Schneider et al. (1991) are selected based on their slitless spectra, and are biased to quasars with stronger emission lines. Sargent, Steidel & Boksenberg (1989) found $\mathrm{EW(Ly}\alpha + \mathrm{NV}) = 80.9 \pm 29.8$ Å for a sample of 59 quasars at $z > 2.75$. Warren, Hewett & Osmer (1994) found a median equivalent width of $\mathrm{EW(Ly}\alpha + \mathrm{NV}) = 68$ Å for quasars at $z > 2.2$. Our result is consistent with these high-redshift samples. At lower redshift, the Large Bright Quasar Survey (LBQS) sample has $\mathrm{EW(Ly}\alpha + \mathrm{NV}) = 52$ Å (Francis et al. 1991).

Schneider et al. (1991) found $\alpha = -0.92 \pm 0.26$, and Sargent, Steidel & Boksenberg (1989) found $\alpha = -0.78 \pm 0.27$, both consistent with our result. Our value is redder than the values found from low redshift samples (e.g., the LBQS sample shows $\alpha_{med} = -0.3$). This could be due to the fact that the α values from low and high redshift samples are based on different wavelength ranges. A detailed comparison of the continuum slope for different redshift ranges would require observations of high-redshift quasars at IR wavelengths. However, our purpose in determining α is to reproduce the true color distribution of the underlying quasar population and thus to calculate the selection function. Since we

measure α by matching to the SDSS photometry, any bias will be small because of the limited wavelength range in the optical spectrum of high-redshift quasars. The difference in the continuum slope between the low and high redshift sample and any deviations of the underlying continuum from a power law, however, will affect the calculation of the K-correction, and the evolution of the luminosity function from $z \lesssim 3$ to $z > 4$ (Paper IV).

5.3. Selection Completeness of the Quasar Sample

In Figure 7, we present the average selection probability for $M_{1450} = -26.5$, as functions of α and EW, $\langle p(\alpha) \rangle$, and $\langle p(\mathrm{EW}) \rangle$, averaged over the survey redshift range $3.6 < z < 5.0$. $\langle p(\alpha) \rangle$ is defined as:

$$\langle p(\alpha) \rangle = \frac{\int_{3.6}^{5.0} p(M_{1450}, z, \alpha) f(\mathrm{EW}) \Psi(M_{1450}, z) \frac{dV(z)}{dz} dz}{\int_{3.6}^{5.0} f(\mathrm{EW}) \Psi(M_{1450}, z) \frac{dV(z)}{dz} dz} \tag{11}$$

where $\Psi(M_{1450}, z) = d\Phi(M_{1450}, z)/dM$ is the differential luminosity function. The quantity $\langle p(\mathrm{EW}) \rangle$ is similarly defined. This figure illustrates the selection completeness as a function of the quasar SED in §5.1 more clearly. On average, the selection criteria are more sensitive to quasars with bluer continua. At this luminosity, where the effects of photometric errors are small, the average selection probability $p \gtrsim 80\%$ for $\alpha > -0.9$, but drops to $\sim 40\%$ for $\alpha = -1.5$, and to $\sim 20\%$ for $\alpha = -2.0$. Note that $\alpha = -1.5$ is about 2 σ away from the mean α. Thus although the current survey is less complete for redder quasars, those objects are not excluded completely and can be corrected for by applying the selection function. The figure also shows that the average selection probability is higher than 80% for quasars with EW > 40 Å, and is still higher than 50% for quasars with much weaker lines, EW $\sim$ 20 Å.

Finally, we calculate the average selection probability of the high-redshift quasars in our sample as a function of redshift and luminosity $p(M_{1450}, z)$, averaging over the α and EW distributions. We calculate the quasar model colors following the same procedures described in §5.1, and assume that the intrinsic properties of quasars follow the distributions we obtained in §5.2. The selection function is calculated for both $\Omega = 1$ and Λ models for $-25 > M_{1450} > -30$ and $3.6 < z < 5.2$.

The results of the selection function are summarized in Figure 8 for both cosmologies. The heavy solid line in the figure represents the 5% contour, indicating the survey limiting absolute magnitude at each redshift. Our survey is cut at $i^* < 20.05$ for *gri* selected quasars, and at $i^* < 20.2$ for *riz* selected quasars. For the $\Omega = 1$ model, the survey reaches $M_{1450} \sim -25.3$ at the lowest redshift $z \sim 3.6$, and to $M_{1450} \sim -25.8$ at $z \sim 4.5$. The

survey then goes slightly deeper at $4.5 < z < 5.0$, due to the fact that our riz selection goes slightly deeper than does the gri selection. Not surprisingly, the survey is more complete for brighter quasars due to smaller photometric errors. The figure indicates that over the entire redshift range between 3.6 and 5.2, the survey is complete to at least 40% for quasars more than ~ 0.4 mag brighter than the survey limit. The main difference between the two cosmologies is a slight shift in the M_{1450} axis.

The survey completeness is a function of redshift: it is most complete in the redshift ranges of 3.8 – 4.2 and 4.7 – 5.2, with $p > 0.8$ for bright quasars. As mentioned in §5.1, the lower completeness at $z \sim 3.6$ is due to the $g^* - r^* > 1.0$ cut in the gri selection. The completeness is lowest at $z \sim 4.4 - 4.5$, about 50% for bright quasars. This is the region in which the Lyα emission moves between the r' and i' filters, and the quasar moves from being selected with the gri selection of Eq. (1) to being selected with the riz selection of Eq. (2). The final quasar target selection algorithm in the SDSS uses a selection in multi-dimensional color space, and is expected to be more complete than the results presented here (see, e.g., Newberg & Yanny 1997).

The locations of the 39 quasars in the sample are also plotted on Figure 8. Note that the average detection probability in Figure 8 is different from the values in Table 4, which is the detection probability for a specific type of intrinsic spectrum. Using the contours in Figure 8, we find an overall average $\langle p(M_{1450}, z)\rangle = 0.75$ for the 39 quasars, which is slightly lower than $\langle p(M_{1450}, z, \alpha, \mathrm{EW})\rangle = 0.80$ we found in §5.1.

6. Summary

In this paper, we present a color-selected flux-limited sample of high-redshift quasars in the Fall Equatorial Stripe that includes 39 quasars at $3.6 < z < 5.0$ and $i^* \lesssim 20$, covering an effective area of 182 deg^2. These objects are identified from 53 quasar candidates, giving a success rate of 73%.

From this sample, we estimate the average power law slope of the quasar spectrum in the rest-frame UV to be -0.79 with a standard deviation of 0.34; and the rest-frame equivalent width of the Lyα+NV emission line to be 69 Å with a standard deviation of 18 Å. These results are consistent with previous high-redshift quasar samples.

We derive the selection function of the survey as a function of redshift, luminosity and the quasar SED shape. We show that on average, the selection criteria are more sensitive to quasars with bluer continua; the survey is incomplete for red quasars with $\alpha < -1.8$. The selection probability does not strongly depend on the quasar emission line strength.

The selection completeness is also a function of redshift. The survey is the most complete in the redshift range from 3.8 to 4.2 and 4.7 – 5.2, while it suffers $\sim 50\%$ incompleteness at $z \sim 4.5$. The average selection probability for the whole sample is $\sim 75\%$. In Paper IV, we use the high-redshift quasar sample and the survey selection function presented in this paper to study the evolution of the quasar luminosity function.

The Sloan Digital Sky Survey (SDSS) is a joint project of the University of Chicago, Fermilab, the Institute for Advanced Study, the Japan Participation Group, The Johns Hopkins University, the Max-Planck-Institute for Astronomy, Princeton University, the United States Naval Observatory, and the University of Washington. Apache Point Observatory, site of the SDSS, is operated by the Astrophysical Research Consortium. Funding for the project has been provided by the Alfred P. Sloan Foundation, the SDSS member institutions, the National Aeronautics and Space Administration, the National Science Foundation, the U.S. Department of Energy, and Monbusho, Japan. The SDSS Web site is `http://www.sdss.org/`. The Hobby-Eberly Telescope (HET) is a joint project of the University of Texas at Austin, the Pennsylvania State University, Stanford University, Ludwig-Maximillians-Universität München, and Georg-August-Universität Göttingen. The HET is named in honor of its principal benefactors, William P. Hobby and Robert E. Eberly. XF and MAS acknowledge support from Research Corporation, NSF grant AST96-16901, the Princeton University Research Board, and a Porter O. Jacobus Fellowship. WHB acknowledges support from the Institute of Geophysics and Planetary Physics (operated under the auspices of the U.S. Department of Energy by the University of California Lawrence Livermore National Laboratory under contract No. W-7405-Eng-48). DPS acknowledges support from NSF grant AST99-00703.

A. Updated SDSS Photometric System Response Function

In Spring 2000, the SDSS photometric system response functions of the photometric camera on the 2.5m telescope were re-measured using a monochrometer. It was found that the passbands of the g', r', i' and z' filters had changed since the filters were measured prior to their installation in the camera in 1997. The major effect is that the red edges of these passbands are at wavelengths 3% bluer than the designed values (Fukugita et al. 1996). For the g', r' and i' filters, the red cutoff is accomplished by an interference coating, whereas the blue cutoff is done by a long-pass colloidal gold-in-glass glass filter. In the SDSS 2.5m imaging camera, the filters are cemented on the back face of the corrector, and the interference films are exposed to the dewar vacuum (Gunn et al. 1998). The most plausible explanation for the change is that the oxide layers in the interference films have

dehydrated in the vacuum and the refractive index of the layers have slightly changed. The manufacturer, Asahi-Spectra Ltd, Tokyo, confirms that this is likely. The change in the z' response is due to the improved measurement of the quantum efficiency at long wavelength for the thick CCDs used in the camera.

Figure A.1 presents the filter response curves for the new and old measurements. Table A.1 gives the effective wavelengths (defined in Eq. 3 in Fukugita et al. 1996) and FWHMs of the SDSS filters of the SDSS 2.5m imaging camera according to the new measurements. Although these new measurements are still preliminary, calculations are carried out with the new system response curve throughout this paper.

B. Faint Quasars from the Fall Equatorial Stripe

The SDSS will image the Fall Equatorial Stripe 35 – 40 times during the five-year survey. Since the Fall Equatorial Stripe is in the southern Galactic Cap, it is called the SDSS Southern Survey (York et al. 2000). The final combined images of the Southern Survey will reach $r' \sim 25$, 2 magnitudes deeper than the main survey. These data will be used to search for fainter quasars, and to study the evolution and large scale distribution of quasars at much lower luminosities. During the commissioning phase of the survey, part of the Fall Equatorial Stripe has been imaged twice. The combined catalog from the two observations is used to select quasar candidates at $i^* < 21$, where the photometric error from a single observation is too large for efficient candidate selection. Eighteen high-redshift quasars are identified from these candidates. The algorithm to combine the imaging data and to search for faint quasar candidates is still under development, and the sample is far from complete. In this Appendix, we simply present the SDSS photometry and the spectra of these 18 quasars, some of which exhibit interesting spectral features.

Table B.1 lists the SDSS imaging runs we used in the selection of faint quasars. The overlapping regions of Runs 94/259 (the Northern Strip of the Stripe, see York et al. 2000) and Runs 125/273 (Southern Strip) were used. Tables B.2, B.3 and B.4, similar to Tables 1, 2 and 3, present the photometry, emission line, and continuum properties of these 18 quasars. In Table B.2, the photometry in both observations are listed; in Table B.4, we do not measure the continuum slope from the photometry, due to the increasing photometric errors, especially in the z' band. Figure B.1 gives the finding charts for these quasars. Figure B.2 presents the spectra. Sixteen of the spectra were obtained with the Keck II/LRIS during the 1999 October observing run. Three of the faint quasars have very poor signal-to-noise ratio beyond 8000 Å thus we do not show this spectral region in the figure. Two objects (SDSSp J024434.87+000124.9 and SDSSp J024452.33–003318.0) were

observed with the ARC 3.5m telescope in 1999 December and 2000 January.

B.1. Note for Individual Objects

SDSSp J010905.81+001617.1 ($z = 3.68$). This has a number of absorption systems in the spectrum, identified both by their C IV λ1548,1551 and Si IV λ1394,1403 absorption lines, including two narrow-line systems, at $z = 3.71$ (higher than the emission-line redshift), and at $z = 3.59$, respectively; and two broad features at $z = 3.43$ (with C IV absorption centered at 6855 Å and Si IV at 6233 Å), and at $z = 3.33$ (with C IV and Si IV absorption at 6700 Å and 6063 Å).

SDSSp J015015.58+004555.7 ($z = 3.91$). This is a BAL quasar, with a velocity (average of C IV and Si IV features) of ~ 7300 km s^{-1}.

SDSSp J023749.33+005715.6 ($z = 3.57$). This quasar has very narrow emission lines. The Lyα and N V emission lines are clearly separated. The Si IV emission line shows two peaks, from the Si IV λ1394, 1403 components. The average FWHM of the emission lines is only ~ 1500 km s^{-1}. Quasars (and Seyfert 1s) with FWHM less than 2000 km s^{-1} are usually classified as Narrow Line Quasars (or Narrow Line Seyfert 1s, which typically have lines broader than Seyfert 2s and with smaller [O III]/Hβ ratio, see, e.g. Baldwin et al. 1988, Osterbrock & Pogge 1985). Those object tend to have strong Fe II emission and soft X-ray spectra, and are thought to be either AGNs with face-on orientation, or represent a higher accretion rate (e.g., Leighly 1999 and reference therein). This is the first narrow line quasar at $z > 3.5$ of which we are aware. A damped Lyα candidate is also detected at $z = 3.26$ ($\lambda = 5177$ Å).

SDSSp J024347.37–010611.7 ($z = 3.90$). The strong absorption at 7268/7286 Å is due to a Mg II absorption system at $z = 1.600$. The total rest-frame equivalent width is 12.3 Å. Absorption lines corresponding to several FeII features at the same redshift are also visible (at 6758Å, 6723Å, 6193Å, 6172Å and 6094 Å).

SDSSp J031427.92+002339.4 ($z = 3.68$). Several metal line systems are detected: two C IV/Si IV systems are at $z = 3.55$ and $z = 3.48$, and there is a Mg II system at $z = 1.11$.

SDSSp J032459.10–005705.1 ($z = 4.80$). This is a very odd-looking high-redshift quasar. The Lyα+N V emission is clearly affected by strong absorption, and the emission line seems very narrow. The O I emission is barely detected, but it is affected by the telluric A-band. The redshift is determined by a fit to the O I line.

SDSSp J033505.43+010337.2 ($z = 3.58$). Most of the rich absorption lines in the

spectrum of this quasar seem to be actually due to one very strong associated absorption system at the same redshift as the emission lines. A entire suite of absorption features due to different ions can be identified, including N V λ1238+1240, Si II λ1260, O I λ1302, Si II λ1304, C II λ1334, Si IV λ1393+1402, Si II λ1526 and C IV λ1548+1550.

REFERENCES

Baldwin, J. A. 1977, ApJ, 214, 679

Baldwin, J. A., McMahon, R., Hazard, C., & Williams, R. E. 1988, ApJ, 327, 103

Becker, R.H., White, R.L., & Helfand, D.J. 1995, ApJ, 450, 559

Dressler, A., & Gunn, J. E. 1982, ApJ, 263, 533

Fan, X. 1999, AJ, 117, 2528

Fan, X. et al., 1999a, AJ, 118, 1 (Paper I)

Fan, X. et al., 1999b, ApJ, 526, L57

Fan, X. et al., 2000a, AJ, 119, 1 (Paper II)

Fan, X. et al., 2000b, AJ, submitted (Paper IV)

Francis, P.J., Hewett, P.C., Foltz, C.B., Chaffee, F.H., Weymann, R.J., & Morris, S.L. 1991, ApJ, 373, 465

Fukugita, M., Ichikawa, T., Gunn, J.E., Doi, M., Shimasaku, K., & Schneider, D.P. 1996, AJ, 111, 1748

Gunn, J.E. et al. 1998, AJ, 116, 3040

Kennefick, J.D., Djorgovski, S.G., & de Carvalho, R.R. 1995, AJ, 110, 255

Leighly, K. M. 1999, ApJS, 125, 317

Lupton, R.H., Gunn, J.E., & Szalay, A. 1999, AJ, 118, 1406

Lupton, R.H. 2000, in preparation

Lupton, R.H., et al. 2000, in preparation

Massey, P. 1988, ApJ, 328, 315

Massey, P., & Cronwall, C. 1990, ApJ, 358, 344

Newberg, H.J., & Yanny, B. 1997, ApJS, 113, 89

Oke, J.B., Cohen, J.G., Carr, M., Cromer, J., Dingizian, A., Harris, F.H., Labrecque, S., Lucinio, R., Schall, W., Epps, H., & Miller, J. 1995, PASP, 107, 375

Osterbrock, D. E., & Pogge, R. W. 1985, ApJ, 297, 166

Poggianti, B. M., Smail, I., Dressler, A., Couch, W. J., Barger, A. J., Butcher, H., Ellis, R. S., & Oemler, A. J. 1999, ApJ, 518, 576

Sargent, W. L. W., Steidel, C. C., & Boksenberg, A. 1989, ApJS, 69, 703

Schlegel, D.J, Finkbeiner, D.P., & Davis, M. 1998, ApJ, 500, 525

Schmidt, M., Schneider, D.P, & Gunn, J.E. 1995, AJ, 110, 68

Schmidt, M., van Gorkom, J. H., Schneider, D. P., & Gunn, J. E. 1995, AJ, 109. 473

Schneider, D. P., Schmidt, M., & Gunn, J.E. 1991, AJ, 102, 837

Schneider, D. P., et al. 2000a, PASP, 112, 6

Schneider, D. P., et al. 2000b, AJ, in press

Schneider, D. P. et al. 2001, in preparation

Siegmund, W. et al. 2000, in preparation

Smith, J. D., Thompson, D., Brisken, W. F., Neugebauer, G., Matthews, K., Meylan, G., Piotto, G., & Suntzeff, N. B. 1994, AJ, 108, 1147

Songaila, A., Hu, E. M., Cowie, L. L., & McMahon, R. G. 1999, ApJ, 525, L5

Stern, D., Djorgovski, S. G., Perley, R. A., de Carvalho, R. R., & Wall, J. V. 2000, AJ, in press

Storrie-Lombardi, L.J., & Irwin, M .J. 1994, ApJ, 427, L13

Voges, W., et al. 1999, A&A, 349, 389

Warren, S.J., Hewett, P., & Osmer, P. S. 1994, ApJ, 421, 412

Weymann, R. J., Morris, S. L., Foltz, C. B., & Hewett, P. C. 1991, ApJ, 373, 2

York, D. G., et al. 2000, AJ, in press

Table 1. Positions and Photometry of Bright SDSS High-redshift Quasars

SDSS name	redshift	u^*	g^*	r^*	i^*	z^*	run
SDSSp J001950.06−004040.9	4.32 ± 0.01	23.60 ± 0.86	21.11 ± 0.05	19.76 ± 0.02	19.61 ± 0.03	19.59 ± 0.10	125
SDSSp J005922.65+000301.4[a]	4.16 ± 0.01	23.68 ± 0.77	22.47 ± 0.16	19.25 ± 0.01	19.18 ± 0.02	19.06 ± 0.07	125
SDSSp J010822.70+001147.9	3.71 ± 0.01	23.25 ± 0.69	20.67 ± 0.03	19.49 ± 0.04	19.44 ± 0.03	19.57 ± 0.11	125
SDSSp J012019.99+000735.5	4.08 ± 0.01	24.73 ± 0.61	21.47 ± 0.06	20.03 ± 0.03	19.84 ± 0.03	20.14 ± 0.17	125
SDSSp J012700.69−004559.1	4.06 ± 0.01	22.99 ± 0.63	19.76 ± 0.02	18.37 ± 0.01	18.10 ± 0.01	18.08 ± 0.02	125
SDSSp J013108.19+005248.2	4.19 ± 0.01	22.88 ± 0.51	22.05 ± 0.10	20.40 ± 0.04	20.05 ± 0.04	20.26 ± 0.15	125
SDSSp J020427.81−011239.6	3.91 ± 0.01	22.53 ± 0.31	20.97 ± 0.04	19.74 ± 0.02	19.65 ± 0.02	19.49 ± 0.07	125
SDSSp J021043.17−001818.4	4.77 ± 0.02	23.77 ± 0.69	22.84 ± 0.17	20.66 ± 0.04	19.25 ± 0.02	19.27 ± 0.06	125
SDSSp J024457.19−010809.9[b]	3.96 ± 0.01	22.72 ± 0.35	20.00 ± 0.02	18.60 ± 0.01	18.38 ± 0.01	18.18 ± 0.02	125
SDSSp J025019.78+004650.3	4.76 ± 0.01	23.90 ± 0.65	22.87 ± 0.17	21.06 ± 0.05	19.67 ± 0.03	19.56 ± 0.09	94
SDSSp J030025.23+003224.2	4.19 ± 0.01	22.74 ± 0.87	21.96 ± 0.09	19.97 ± 0.02	19.96 ± 0.03	19.75 ± 0.08	125
SDSSp J030707.46−001601.4	3.70 ± 0.01	22.75 ± 0.46	21.24 ± 0.05	20.03 ± 0.02	19.95 ± 0.03	20.07 ± 0.13	125
SDSSp J035214.33−001941.1	4.18 ± 0.01	23.83 ± 0.72	21.73 ± 0.08	20.11 ± 0.02	19.73 ± 0.03	19.58 ± 0.09	125
SDSSp J040550.26+005931.2	4.05 ± 0.01	22.59 ± 0.46	22.30 ± 0.12	20.22 ± 0.03	20.01 ± 0.04	19.65 ± 0.09	125
SDSSp J232717.99+000546.1	3.66 ± 0.01	24.67 ± 0.77	20.92 ± 0.04	19.89 ± 0.03	19.85 ± 0.04	19.95 ± 0.16	125
SDSSp J235053.55−004810.3	3.85 ± 0.01	23.60 ± 0.86	21.11 ± 0.05	19.76 ± 0.02	19.61 ± 0.03	19.59 ± 0.10	125

Positions are in J2000.0 coordinates; asinh magnitudes (Lupton, Gunn & Szalay 1999) are quoted; errors are statistical only. For reference, zero flux corresponds to asinh magnitudes of 23.40, 24.22, 23.98, 23.51, and 21.83 in u^*, g^*, r^*, i^*, and z^*, respectively.

[a]This is the previously known quasar PSS 0059+0003 (Kennefick et al. 1995)

[b]This quasar was first reported at http://astro.caltech.edu/~george/z4.qsos as PSS 0244-0108

Table 2. Emission Line Properties of Bright SDSS High−redshift Quasars

quasar	O VI 1034	Lyα 1216 + 1240	O I+Si II 1306	Si IV+O IV] 1402	C IV 1549
SDSSp J001950.06−004040.9	...	6637.1 ± 4.0	7443.9 ± 7.4	6948.3 ± 6.9	8247 ± 7.7
	...	53.5 ± 0.8	1.4 ± 0.6	3.3 ± 0.7	13.4 ± 2.6
SDSSp J010822.70+001147.9	...	5728.2 ± 0.1	6151.2 ± 2.3	6572.2 ± 2.0	7281 ± 0.8
	...	74.6 ± 0.6	2.1 ± 0.3	6.6 ± 0.4	30.3 ± 0.8
SDSSp J012019.99+000735.5	5275.5 ± 0.6	6191.2 ± 0.5	6647.5 ± 2.4	711.4 ± 3.1	7868 ± 1.1
	23.0 ± 0.6	82.9 ± 1.0	3.8 ± 0.5	7.3 ± 0.9	31.6 ± 1.0
SDSSp J012700.69−004559.1	5226.5 ± 0.2	6194.1 ± 0.1	...	7192.5 ± 0.5	7840 ± 0.3
	14.9 ± 0.1	93.5 ± 0.1	...	14.1 ± 0.2	33.2 ± 0.2
SDSSp J013108.19+005248.2	5369.5 ± 1.1	6320.2 ± 0.2	6779.1 ± 2.5	7266.7 ± 3.3	8046 ± 0.9
	19.1 ± 0.9	71.6 ± 1.8	5.1 ± 0.7	7.5 ± 0.8	25.0 ± 0.9
SDSSp J020427.81−011239.6	...	6007.1 ± 0.5	6435.5 ± 2.0	6893.8 ± 2.4	7592 ± 1.8
	...	71.1 ± 0.5	4.2 ± 0.4	11.6 ± 0.7	25.0 ± 1.2
SDSSp J021043.17−001818.4	...	7019.6 ± 0.8	...	...	...
	...	42.5 ± 0.7	...	...	...
SDSSp J024457.19−010809.9	...	6121.1 ± 0.8	...	6950.8 ± 6.5	7691 ± 2.8
	...	87.9 ± 0.9	...	11.0 ± 0.9	36.7 ± 1.1
SDSSp J025019.78+004650.3	...	7034.1 ± 0.7	...	8068.6 ± 3.0	...
	...	42.8 ± 1.0	...	4.1 ± 0.4	...
SDSSp J030025.23+003224.2	5350.0 ± 0.2	6309.2 ± 0.1	6774.2 ± 2.5	7259.2 ± 3.0	8038 ± 0.4
	16.4 ± 0.2	114.7 ± 0.7	2.4 ± 0.3	9.2 ± 0.7	33.1 ± 0.4
SDSSp J030707.46−001601.4	...	5717.5 ± 0.2	6135.9 ± 0.9	6586.9 ± 1.4	7270 ± 0.7
	...	60.3 ± 0.7	5.6 ± 0.2	11.0 ± 0.5	13.7 ± 0.2
SDSSp J035214.33−001941.1	...	6321.9 ± 0.4	6783.3 ± 3.7	7256.5 ± 2.6	8015 ± 2.3
	...	108.3 ± 1.6	1.9 ± 0.6	8.3 ± 0.8	17.9 ± 0.1
SDSSp J040550.26+005931.2	...	6144.5 ± 0.1	6593.8 ± 2.1	7073.0 ± 2.0	7826 ± 0.5
	...	95.3 ± 1.2	3.8 ± 0.4	6.0 ± 0.4	30.3 ± 0.4
SDSSp J232717.99+000546.1	...	5687.0 ± 0.9	...	6538.0 ± 3.6	7219 ± 1.1
	...	50.6 ± 0.7	...	7.4 ± 0.9	18.9 ± 0.7
SDSSp J235053.55−004810.3	...	5934.4 ± 0.7	6334.1 ± 3.3	6810.4 ± 3.6	7501 ± 2.3
	...	52.8 ± 0.6	9.3 ± 2.1	7.8 ± 0.8	15.1 ± 0.6

The two entries in each line are the central wavelength and rest frame equivalent width from the Gaussian fit to the line profile, both measured in Ångstroms.

Table 3. Continuum Properties of Bright SDSS High−redshift Quasars

quasar	redshift	E(B−V)	AB_{1450}	M_{1450}	α
SDSSp J001950.06−004040.9	4.32 ± 0.01	0.027	19.62 ± 0.05	−26.36	−0.02 ± 0.62
SDSSp J005922.65+000301.4	4.16 ± 0.01	0.025	19.30 ± 0.03	−26.62	−1.09 ± 0.33
SDSSp J010822.70+001147.9	3.71 ± 0.01	0.029	19.62 ± 0.04	−26.12	−0.19 ± 0.24
SDSSp J012019.99+000735.5	4.08 ± 0.01	0.037	19.96 ± 0.04	−25.93	−0.52 ± 0.30
SDSSp J012700.69−004559.1	4.06 ± 0.01	0.031	18.28 ± 0.02	−27.60	−0.66 ± 0.13
SDSSp J013108.19+005248.2	4.19 ± 0.01	0.022	20.17 ± 0.04	−25.76	0.11 ± 0.34
SDSSp J020427.81−011239.6	3.91 ± 0.01	0.026	19.80 ± 0.03	−26.02	−0.83 ± 0.17
SDSSp J021043.17−001818.4	4.77 ± 0.02	0.029	19.33 ± 0.07	−26.80	0.06 ± 0.41
SDSSp J024457.19−010809.9	3.96 ± 0.01	0.030	18.46 ± 0.02	−27.38	−1.21 ± 0.11
SDSSp J025019.78+004650.3	4.76 ± 0.01	0.052	19.64 ± 0.08	−26.49	−0.59 ± 0.57
SDSSp J030025.23+003224.2	4.19 ± 0.01	0.095	19.96 ± 0.04	−25.97	−0.99 ± 0.24
SDSSp J030707.46−001601.4	3.70 ± 0.01	0.063	20.04 ± 0.03	−25.69	−0.71 ± 0.21
SDSSp J035214.33−001941.1	4.18 ± 0.01	0.167	19.51 ± 0.03	−26.42	−0.16 ± 0.23
SDSSp J040550.26+005931.2	4.05 ± 0.01	0.444	19.27 ± 0.04	−26.61	−0.48 ± 0.21
SDSSp J232717.99+000546.1	3.66 ± 0.01	0.036	19.93 ± 0.04	−25.78	−0.15 ± 0.20
SDSSp J235053.55−004810.3	3.85 ± 0.01	0.027	19.80 ± 0.03	−26.00	−0.89 ± 0.20

Absolute magnitudes assume $H_0 = 50\,\mathrm{km\,s^{-1}\,Mpc^{-1}}$ and $\Omega_m = 1$

Table 4. Color Selected Sample of 182 deg^2 in Fall Equatorial Stripe

quasar	redshift	AB_{1450}	M_{1450}	α	EW(Lyα + NV)	p
SDSS J001950.06-004040.9	4.32	19.62 ± 0.05	−26.36	−0.02 ± 0.62	53.5	0.90
SDSS J003525.29+004002.8	4.75	19.96 ± 0.08	−26.16	−0.84 ± 0.60	82.4	0.99
SDSS J005922.65+000301.4	4.16	19.30 ± 0.03	−26.62	−1.09 ± 0.33	77.1	0.78
SDSS J010619.25+004823.4	4.43	18.69 ± 0.04	−27.33	−0.40 ± 0.31	69.6	0.74
SDSS J010822.70+001147.9	3.71	19.62 ± 0.04	−26.12	−0.19 ± 0.24	74.6	0.98
SDSS J012019.99+000735.5	4.08	19.96 ± 0.04	−25.93	−0.52 ± 0.30	82.9	0.95
SDSS J012403.78+004432.7	3.81	18.07 ± 0.02	−27.71	−0.44 ± 0.11	74.2	0.98
SDSS J012650.77+011611.8	3.66	19.53 ± 0.03	−26.19	−0.35 ± 0.19	76.0	0.84
SDSS J012700.69-004559.1	4.06	18.28 ± 0.02	−27.60	−0.66 ± 0.13	93.5	0.98
SDSS J013108.19+005248.2	4.19	20.17 ± 0.04	−25.76	0.11 ± 0.34	71.6	0.42
SDSS J015048.83+004126.2	3.67	18.39 ± 0.02	−27.33	−0.52 ± 0.12	47.9	0.82
SDSS J015339.61-001104.9	4.20	18.90 ± 0.02	−27.03	−1.32 ± 0.33	69.3	0.55
SDSS J020427.81-011239.6	3.91	19.80 ± 0.03	−26.02	−0.83 ± 0.17	71.1	0.84
SDSS J020731.68+010348.9	3.85	20.10 ± 0.04	−25.70	−1.00 ± 0.21	60.2	0.56
SDSS J021043.17-001818.4	4.77	19.33 ± 0.07	−26.80	0.06 ± 0.41	42.5	0.97
SDSS J021102.72-000910.3	4.90	19.93 ± 0.10	−26.24	−0.99 ± 0.70	60.9	1.00
SDSS J023231.40-000010.7	3.81	19.82 ± 0.03	−25.96	−0.44 ± 0.18	48.6	0.91
SDSS J023908.98-002121.5	3.74	19.60 ± 0.03	−26.15	−0.78 ± 0.16	65.8	0.89
SDSS J024457.19-010809.9	3.96	18.46 ± 0.02	−27.38	−1.21 ± 0.11	87.9	0.64
SDSS J025019.78+004650.3	4.76	19.64 ± 0.08	−26.49	−0.59 ± 0.57	42.8	0.99
SDSS J025112.44-005208.2	3.78	19.49 ± 0.03	−26.28	0.05 ± 0.49	75.1	0.89
SDSS J030025.23+003224.2	4.19	19.96 ± 0.04	−25.97	−0.99 ± 0.24	114.7	0.91
SDSS J030707.46-001601.4	3.70	20.04 ± 0.03	−25.69	−0.71 ± 0.21	60.3	0.76
SDSS J031036.85+005521.7	3.77	19.25 ± 0.03	−26.51	−0.64 ± 0.15	45.0	0.83
SDSS J031036.97-001457.0	4.63	20.03 ± 0.07	−26.05	−0.02 ± 0.65	56.9	0.97
SDSS J032608.12-003340.2	4.16	19.14 ± 0.03	−26.78	−0.33 ± 0.18	58.8	1.00
SDSS J033829.31+002156.3	5.00	19.73 ± 0.12	−26.47	−0.81 ± 0.76	71.5	0.98
SDSS J033910.53-003009.2	3.74	19.93 ± 0.03	−25.82	−1.17 ± 0.20	74.7	0.69
SDSS J035214.33-001941.1	4.18	19.51 ± 0.03	−26.42	−0.16 ± 0.23	108.3	0.99
SDSS J225419.23-000155.0	3.68	19.41 ± 0.03	−26.31	−0.95 ± 0.17	87.2	0.78
SDSS J225452.88+004822.7	3.69	20.24 ± 0.04	−25.49	−1.51 ± 0.27	95.6	0.31
SDSS J225529.09-003433.4	4.08	20.26 ± 0.06	−25.63	−1.15 ± 0.37	82.8	0.52
SDSS J225759.67+001645.7	3.75	19.06 ± 0.02	−26.69	−0.58 ± 0.15	72.3	0.96
SDSS J230323.77+001615.2	3.68	20.24 ± 0.04	−25.48	−0.77 ± 0.26	107.1	0.56
SDSS J230639.65+010855.2	3.64	19.14 ± 0.03	−26.57	−1.38 ± 0.15	57.5	0.45
SDSS J230952.29-003138.9	3.95	19.50 ± 0.03	−26.34	−0.72 ± 0.18	63.8	0.94
SDSS J232208.22-005235.2	3.84	20.19 ± 0.04	−25.60	−1.18 ± 0.24	59.6	0.73
SDSS J235053.55-004810.3	3.85	19.80 ± 0.03	−26.00	−0.89 ± 0.20	52.8	0.76
SDSS J235718.35+004350.4	4.34	19.87 ± 0.05	−26.11	−1.08 ± 0.65	47.1	0.38

Absolute magnitudes assume $H_0 = 50\,\mathrm{km\,s^{-1}\,Mpc^{-1}}$ and $\Omega_m = 1$

Table A1. New SDSS Filter Characteristics of the SDSS 2.5m Imaging Camera, for 1.2 Air Mass

	u'	g'	r'	i'	z'
λ_{eff} (Å)	3561	4676	6176	7494	8873
FWHM (Å)	560	1270	1130	1270	950

Table B1. Summary of SDSS Photometric Runs

Run	Date	Stripe	RA Range	Seeing (arcsec)
94	1998 Sep 19	North	$335.38 - 58.92$	1.5
125	1998 Sep 22	South	$349.51 - 76.00$	1.6
259	1998 Nov 17	North	$7.27 - 96.04$	$2.0 - 1.0$
273	1998 Nov 19	South	$10.55 - 91.57$	$1.6 - 1.4$

Table B2. Positions and Photometry of Faint SDSS High-redshift Quasars

SDSS name	redshift	u^*	g^*	r^*	i^*	z^*	run
SDSSp J004154.38−002955.9	3.82 ± 0.01	23.88 ± 0.70	21.66 ± 0.06	20.45 ± 0.03	20.35 ± 0.04	20.29 ± 0.16	94
		23.16 ± 1.00	21.91 ± 1.08	20.51 ± 0.06	20.42 ± 0.10	19.99 ± 0.25	259
SDSSp J005129.39−003644.7	3.71 ± 0.01	23.54 ± 0.60	21.75 ± 0.07	20.38 ± 0.03	20.23 ± 0.04	20.48 ± 0.19	94
		23.34 ± 1.06	21.76 ± 0.16	20.46 ± 0.08	20.50 ± 0.14	21.14 ± 0.65	259
SDSSp J005348.66−002157.2	3.98 ± 0.02	24.42 ± 0.67	22.09 ± 0.12	20.43 ± 0.03	20.36 ± 0.05	20.60 ± 0.22	125
		23.26 ± 0.64	22.00 ± 0.14	20.65 ± 0.05	20.73 ± 0.08	20.90 ± 0.41	273
SDSSp J005452.86−001344.6	3.74 ± 0.01	23.58 ± 0.80	21.26 ± 0.06	20.18 ± 0.03	20.16 ± 0.04	20.13 ± 0.14	125
		23.96 ± 0.81	21.30 ± 0.07	20.30 ± 0.05	20.21 ± 0.06	20.22 ± 0.26	273
SDSSp J010905.81+001617.1	3.68 ± 0.01	24.16 ± 0.55	21.99 ± 0.07	20.79 ± 0.04	20.69 ± 0.06	21.34 ± 0.43	94
		24.38 ± 1.09	22.28 ± 0.18	20.91 ± 0.09	20.94 ± 0.16	20.74 ± 0.40	259
SDSSp J015015.58+004555.7	3.91 ± 0.01	24.47 ± 0.54	22.33 ± 0.10	20.80 ± 0.04	20.54 ± 0.05	20.51 ± 0.20	94
		23.40 ± 0.71	22.12 ± 0.13	20.78 ± 0.06	20.58 ± 0.07	20.36 ± 0.16	259
SDSSp J023749.33+005715.6	3.57 ± 0.01	22.85 ± 0.47	21.67 ± 0.07	20.60 ± 0.04	20.59 ± 0.06	20.57 ± 0.19	125
		23.20 ± 0.76	21.69 ± 0.10	20.50 ± 0.05	20.46 ± 0.08	20.55 ± 0.34	273
SDSSp J023935.25+010256.9	4.04 ± 0.01	23.46 ± 0.70	22.15 ± 0.10	20.86 ± 0.05	20.76 ± 0.06	20.29 ± 0.18	125
		24.16 ± 0.78	22.27 ± 0.17	20.67 ± 0.06	20.52 ± 0.09	21.03 ± 0.50	273
SDSSp J024347.37−010611.7	3.90 ± 0.01	22.69 ± 0.35	21.99 ± 0.11	20.39 ± 0.03	20.27 ± 0.04	20.04 ± 0.12	125
		24.54 ± 0.81	21.83 ± 0.10	20.27 ± 0.05	20.27 ± 0.06	19.94 ± 0.18	273
SDSSp J024434.87+000124.9	3.76 ± 0.01	23.19 ± 0.60	21.85 ± 0.08	20.49 ± 0.03	20.43 ± 0.04	20.36 ± 0.20	125
		23.64 ± 0.72	21.88 ± 0.11	20.63 ± 0.05	20.43 ± 0.06	20.25 ± 0.25	273
SDSSp J024452.33−003318.0	3.97 ± 0.01	23.44 ± 0.56	21.94 ± 0.07	20.40 ± 0.03	20.29 ± 0.04	20.06 ± 0.13	94
		23.79 ± 0.60	21.98 ± 0.08	20.38 ± 0.05	20.28 ± 0.05	20.10 ± 0.15	259
SDSSp J031427.92+002339.4	3.68 ± 0.01	24.25 ± 0.59	21.67 ± 0.06	20.44 ± 0.03	20.37 ± 0.04	20.22 ± 0.20	94
		24.68 ± 0.60	21.78 ± 0.08	20.38 ± 0.05	20.45 ± 1.08	20.32 ± 0.20	259
SDSSp J032459.10−005705.1	4.80 ± 0.02	23.12 ± 0.45	25.09 ± 0.72	22.73 ± 0.22	20.70 ± 0.06	20.31 ± 0.18	94
		23.99 ± 0.81	25.27 ± 0.84	22.51 ± 0.27	20.51 ± 0.07	20.48 ± 0.26	259
SDSSp J033414.10+004056.6	4.33 ± 0.01	24.44 ± 0.62	23.31 ± 0.25	21.20 ± 0.06	20.82 ± 0.07	20.75 ± 0.26	94
		24.19 ± 0.82	23.44 ± 0.44	21.14 ± 0.08	20.91 ± 0.09	20.51 ± 0.19	259
SDSSp J033505.43+010337.2	3.58 ± 0.01	22.66 ± 0.37	22.35 ± 1.06	20.71 ± 0.04	20.55 ± 0.06	20.06 ± 0.15	94
		23.46 ± 0.83	22.23 ± 0.16	20.67 ± 0.06	20.49 ± 0.07	20.49 ± 0.23	259
SDSSp J042244.38−001247.8	4.09 ± 0.01	23.66 ± 0.69	22.40 ± 0.13	20.85 ± 0.04	20.46 ± 0.04	20.52 ± 0.17	125
		23.19 ± 0.56	22.46 ± 0.17	20.77 ± 0.06	20.51 ± 0.07	20.33 ± 0.24	273
SDSSp J042911.48+003501.7	3.74 ± 0.01	23.88 ± 0.66	23.26 ± 0.25	21.07 ± 0.05	20.65 ± 0.05	20.57 ± 0.17	125
		24.45 ± 0.70	23.33 ± 0.37	21.12 ± 0.08	20.68 ± 0.07	20.82 ± 0.27	273
SDSSp J043649.87−010612.9	3.99 ± 0.02	24.60 ± 0.55	21.84 ± 0.08	20.46 ± 0.03	20.24 ± 0.04	20.25 ± 0.13	125
		24.02 ± 0.05	21.76 ± 0.09	20.39 ± 0.05	20.12 ± 0.05	20.32 ± 0.24	273

Positions are in J2000.0 coordinates; asinh magnitudes (Lupton, Gunn & Szalay 1999) are quoted; errors are statistical only. For reference, zero flux corresponds to asinh magnitudes of 23.40, 24.22, 23.98, 23.51, and 21.83 in u^*, g^*, r^*, i^*, and z^*, respectively.

Table B3. Emission Line Properties of Faint SDSS High−redshift Quasars

quasar	O VI 1034	Lyα 1216 + 1240	O I+Si II 1306	Si IV+O IV] 1402	C IV 1549
SDSSp J004154.38−002955.9	...	5890.3 ± 1.6	...	6756.3 ± 4.7	7467 ± 4.6
	...	60.6 ± 2.2	...	7.1 ± 1.1	29.4 ± 5.9
SDSSp J005129.39−003644.7	...	5749.8 ± 0.5	6163.9 ± 2.4	6608.2 ± 3.1	7298 ± 1.4
	...	110.0 ± 2.0	3.8 ± 0.8	14.9 ± 1.7	36.3 ± 2.2
SDSSp J005348.66−002157.2	5147.4 ± 0.7	6064.3 ± 0.1	6509.9 ± 2.7	6959.9 ± 2.8	7746 ± 5.7
	16.8 ± 0.5	59.2 ± 0.7	4.5 ± 0.9	5.5 ± 0.8	50.4 ± 4.6
SDSSp J005452.86−001344.6	4904.0 ± 1.3	5785.4 ± 0.2	6220.1 ± 5.0	6648.8 ± 2.2	7352 ± 0.9
	25.7 ± 0.8	52.4 ± 0.9	1.9 ± 0.4	7.2 ± 0.5	24.3 ± 0.8
SDSSp J010905.81+001617.1	...	5791.6 ± 0.6	...	6547.1 ± 4.0	7251 ± 1.2
	...	110.6 ± 0.7	...	8.1 ± 0.5	13.0 ± 0.6
SDSSp J015015.58+004555.7	5067.0 ± 0.6	...	...	6883.3 ± 2.2	7608 ± 1.6
	8.6 ± 0.2	...	...	17.2 ± 0.5	22.6 ± 0.5
SDSSp J023749.33+005715.6	...	5563.4 ± 0.1	5977.1 ± 3.0	6389.9 ± 2.8	7082 ± 0.6
	...	21.3 ± 0.2	2.5 ± 0.4	7.0 ± 0.6	8.3 ± 0.3
SDSSp J023935.25+010256.9	...	6156.5 ± 0.2	6603.1 ± 2.0	7072.0 ± 2.2	7816 ± 1.1
	...	73.1 ± 0.8	3.8 ± 0.3	15.5 ± 1.4	42.1 ± 1.6
SDSSp J024347.37−010611.7	...	5979.2 ± 3.7	6415.2 ± 1.5	6864.2 ± 2.0	7553 ± 1.1
	...	108.8 ± 1.7	3.9 ± 0.3	12.1 ± 0.7	11.7 ± 0.4
SDSSp J024434.87+000124.9	...	5866.0 ± 6.4	...	...	7370 ± 16.6
	...	114.0 ± 16.1	...	...	31.3 ± 5.8
SDSSp J024452.33−003318.0	...	6043.3 ± 1.9	...	...	...
	...	55.9 ± 5.7	...	...	...
SDSSp J031427.92+002339.4	...	5697.2 ± 0.1	6117.6 ± 1.9	6548.0 ± 2.8	7248 ± 0.4
	...	53.2 ± 0.8	2.1 ± 0.2	5.7 ± 0.4	24.3 ± 0.3
SDSSp J032459.10−005705.1	...	7042.9 ± 0.2	7578.3 ± 3.7	...	...
	...	42.8 ± 0.3	3.7 ± 0.7	...	...
SDSSp J033414.10+004056.6	5512.8 ± 1.4	6493.1 ± 0.2	6956.1 ± 2.3	7458.7 ± 3.0	8258 ± 1.1
	22.3 ± 1.0	56.8 ± 1.1	3.1 ± 0.3	8.4 ± 0.8	26.3 ± 1.2
SDSSp J033505.43+010337.2	...	...	5981.9 ± 1.2	6419.9 ± 2.9	7100 ± 1.7
	...	...	6.5 ± 0.6	3.3 ± 0.4	11.8 ± 0.4
SDSSp J042244.38−001247.8	...	6186.5 ± 0.1	6662.3 ± 1.9	7124.7 ± 2.6	7875 ± 0.9
	...	49.7 ± 0.8	2.2 ± 0.2	10.0 ± 0.6	23.9 ± 0.5
SDSSp J042911.48+003501.7	4903.0 ± 0.9	5768.2 ± 0.1	6182.5 ± 1.3	6634.0 ± 3.4	7342 ± 0.3
	29.4 ± 2.0	116.3 ± 2.1	6.0 ± 0.4	8.1 ± 0.9	46.3 ± 0.6
SDSSp J043649.87−010612.9	...	6151.5 ± 1.0	6561.5 ± 4.6	6996.2 ± 6.0	7722 ± 2.8
	...	81.0 ± 1.0	5.2 ± 1.7	8.6 ± 0.8	25.7 ± 1.1

The two entries in each line are the central wavelength and rest frame equivalent width from the Gaussian fit to the line profile, both measured in Ångstroms.

Table B4. Continuum Properties of Faint SDSS High−redshift Quasars

quasar	redshift	$E(B-V)$	AB_{1450}	M_{1450}
SDSSp J004154.38−002955.9	3.82 ± 0.01	0.021	20.50 ± 0.04	−25.28
SDSSp J005129.39−003644.7	3.71 ± 0.01	0.051	20.49 ± 0.04	−25.25
SDSSp J005348.66−002157.2	3.98 ± 0.02	0.026	20.55 ± 0.05	−25.30
SDSSp J005452.86−001344.6	3.74 ± 0.01	0.025	20.31 ± 0.04	−25.44
SDSSp J010905.81+001617.1	3.68 ± 0.01	0.026	20.89 ± 0.05	−24.83
SDSSp J015015.58+004555.7	3.91 ± 0.01	0.029	20.58 ± 0.05	−25.24
SDSSp J023749.33+005715.6	3.57 ± 0.01	0.032	20.67 ± 0.05	−25.00
SDSSp J023935.25+010256.9	4.04 ± 0.01	0.031	20.95 ± 0.06	−24.92
SDSSp J024347.37−010611.7	3.90 ± 0.01	0.032	20.38 ± 0.04	−25.44
SDSSp J024434.87+000124.9	3.76 ± 0.01	0.030	20.64 ± 0.04	−25.12
SDSSp J024452.33−003318.0	3.97 ± 0.01	0.030	20.36 ± 0.04	−25.48
SDSSp J031427.92+002339.4	3.68 ± 0.01	0.098	20.33 ± 0.04	−25.39
SDSSp J032459.10−005705.1	4.80 ± 0.02	0.099	20.53 ± 0.14	−25.61
SDSSp J033414.10+004056.6	4.33 ± 0.01	0.132	20.69 ± 0.10	−25.29
SDSSp J033505.43+010337.2	3.58 ± 0.01	0.100	20.46 ± 0.05	−25.22
SDSSp J042244.38−001247.8	4.09 ± 0.01	0.071	20.50 ± 0.05	−25.40
SDSSp J042911.48+003501.7	3.74 ± 0.01	0.075	21.02 ± 0.06	−24.73
SDSSp J043649.87−010612.9	3.99 ± 0.02	0.037	20.37 ± 0.04	−25.48

Absolute magnitudes assume $H_0 = 50\,\mathrm{km\,s^{-1}\,Mpc^{-1}}$ and $\Omega_m = 1$

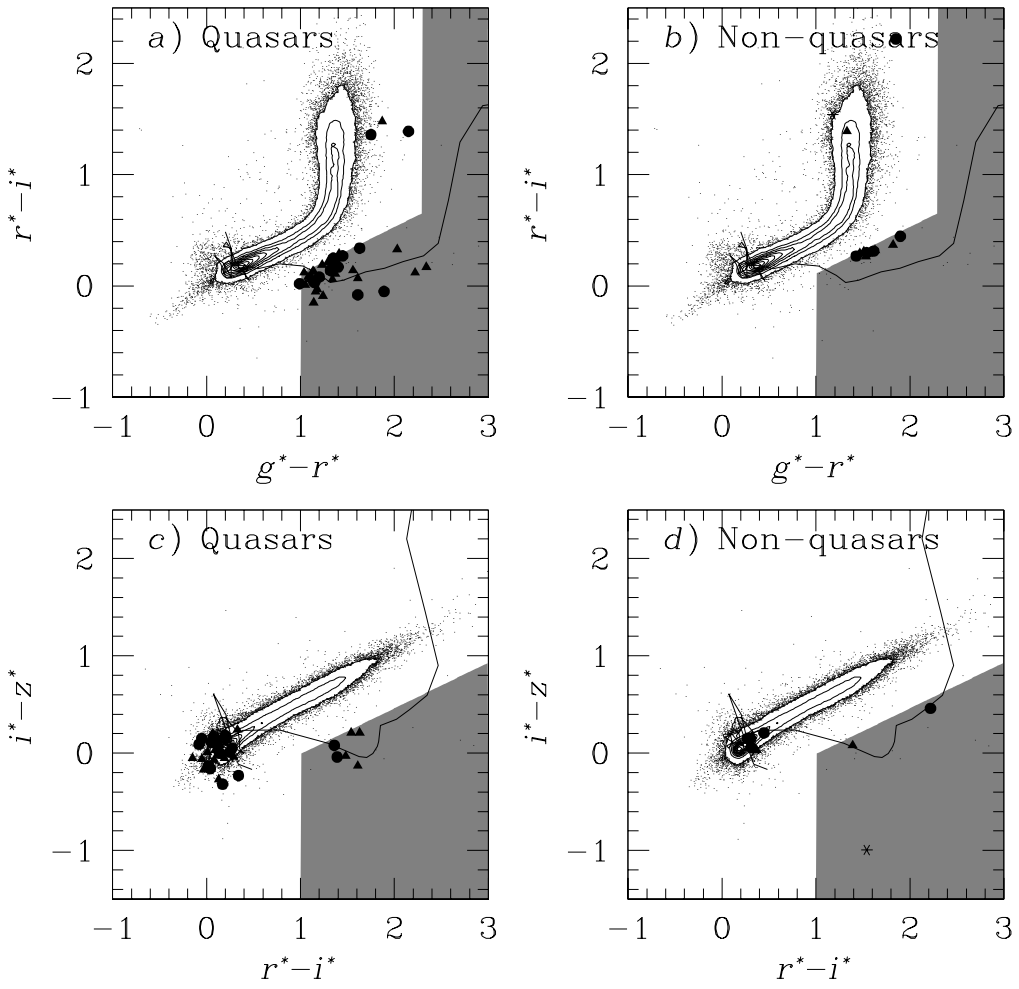

Figure 1. Color-color diagrams for all stellar objects with $i^* < 20.2$ in 25 square degrees of SDSS imaging data. The inner parts of the diagrams are shown as contours, linearly spaced in the density of stars in color-color space. The shaded areas on the $g^* - r^*$ vs. $r^* - i^*$ and the $r^* - i^*$ vs. $i^* - z^*$ diagrams represent the selection criteria used to select quasar candidates. The solid line is the median track of simulated quasar colors as a function of redshift (adapted from Fan 1999). (a) and (c) show the colors of 39 quasars at $z > 3.6$ in the complete sample. The circles are new quasars presented in this paper; the triangles are quasars presented in Fan et al. (1999a) and Schneider et al. (2000b). (b) and (d) shows the colors of 14 non-quasars that satisfy the selection criteria. The circles are objects identified as galaxies; the triangles are stars; and the asterisks are objects with unidentified spectra.

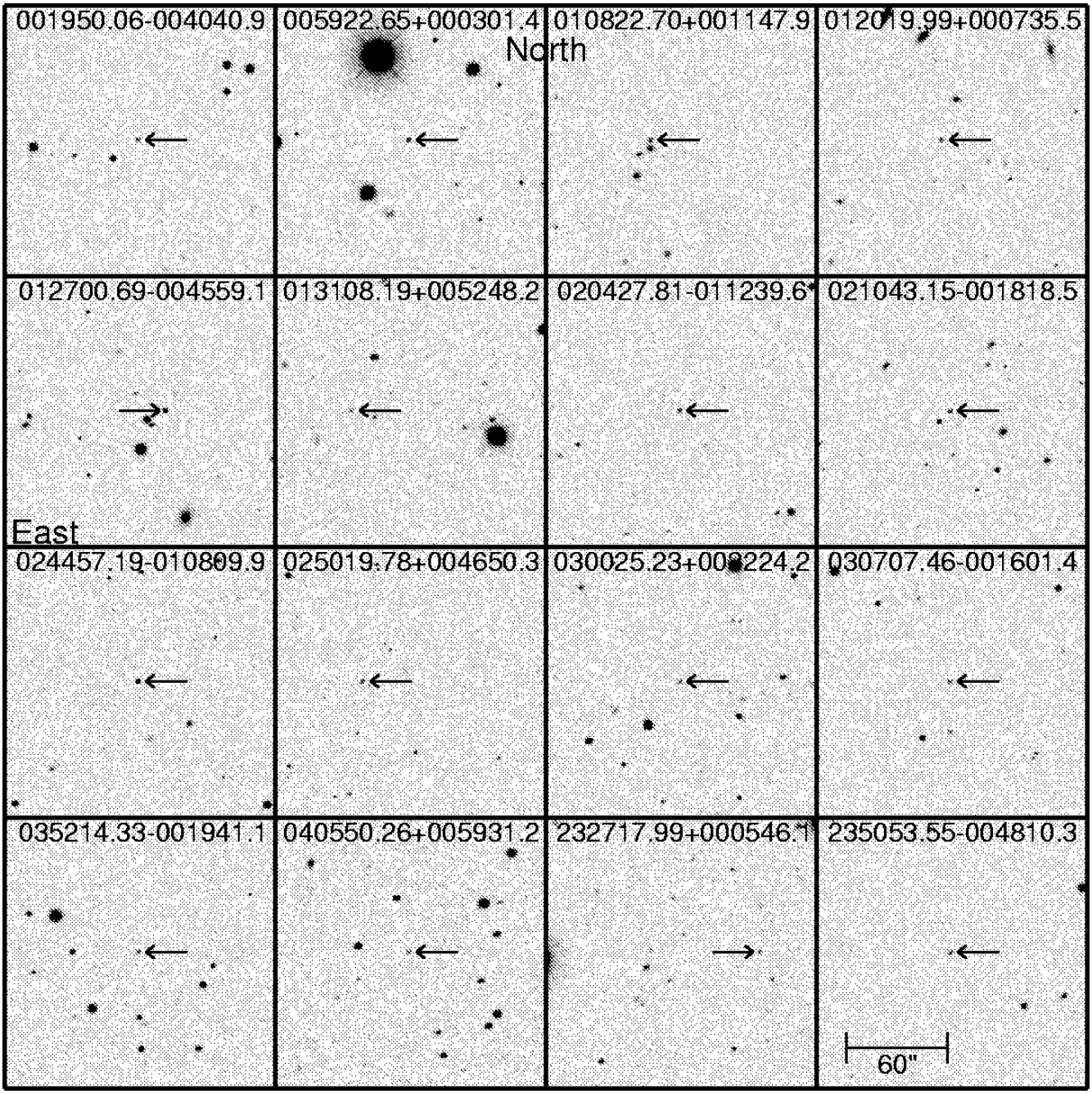

Figure 2. Finding charts for the 16 bright SDSS quasars. The data are $160'' \times 160''$ SDSS images in the i' band (54.1 sec exposure time). Most of them are re-constructed from the atlas images and binned background from the SDSS database. North is up; East is to the left.

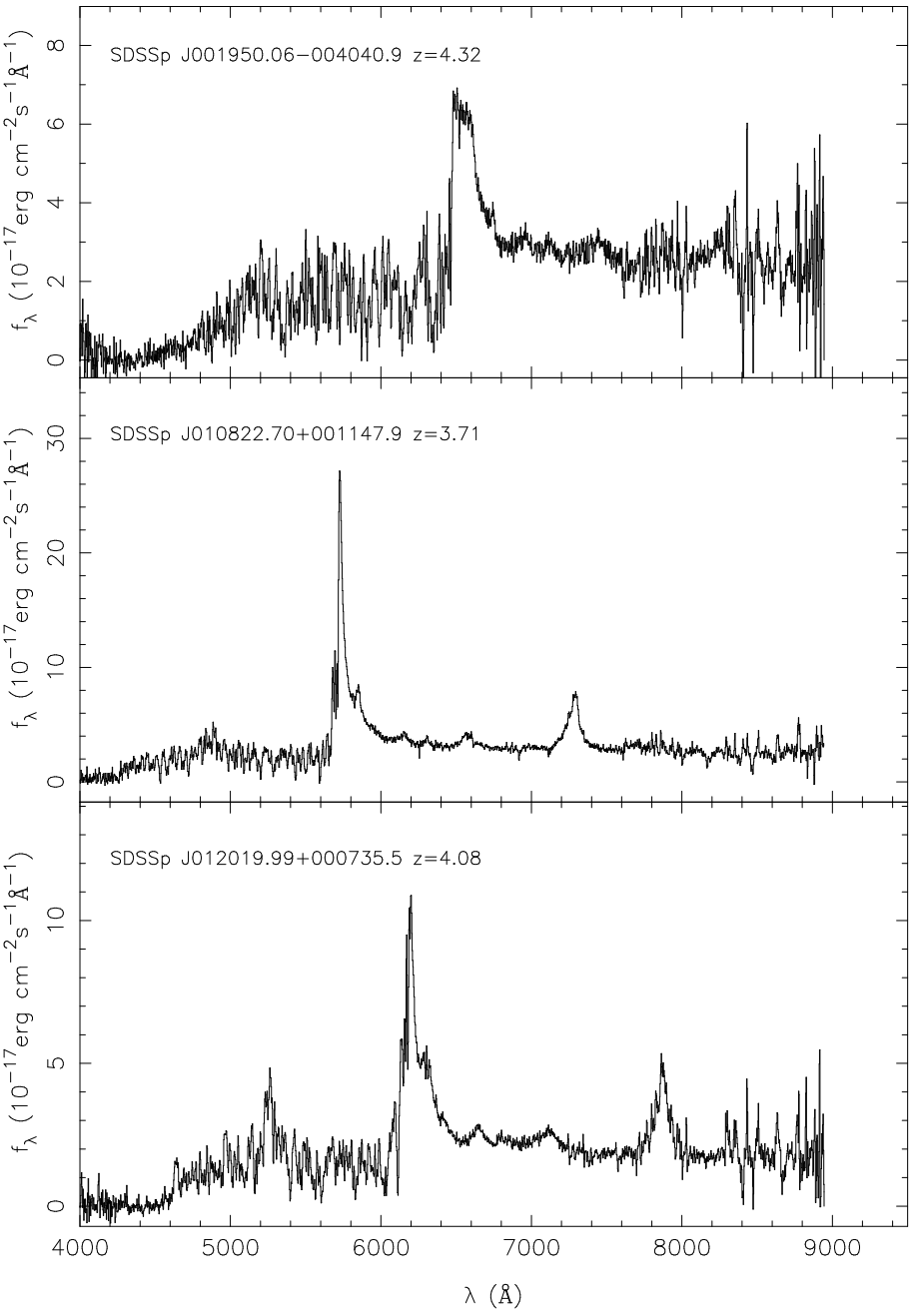

Figure 3. Spectra of 15 bright SDSS quasars. Most are Keck II/LRIS spectra with a dispersion of 2 Å/pixel. The spectrum of SDSSp J024457.19–010809.9 (PSS 0244–0108) was taken with the ARC 3.5m at a dispersion of 6Å/pixel.

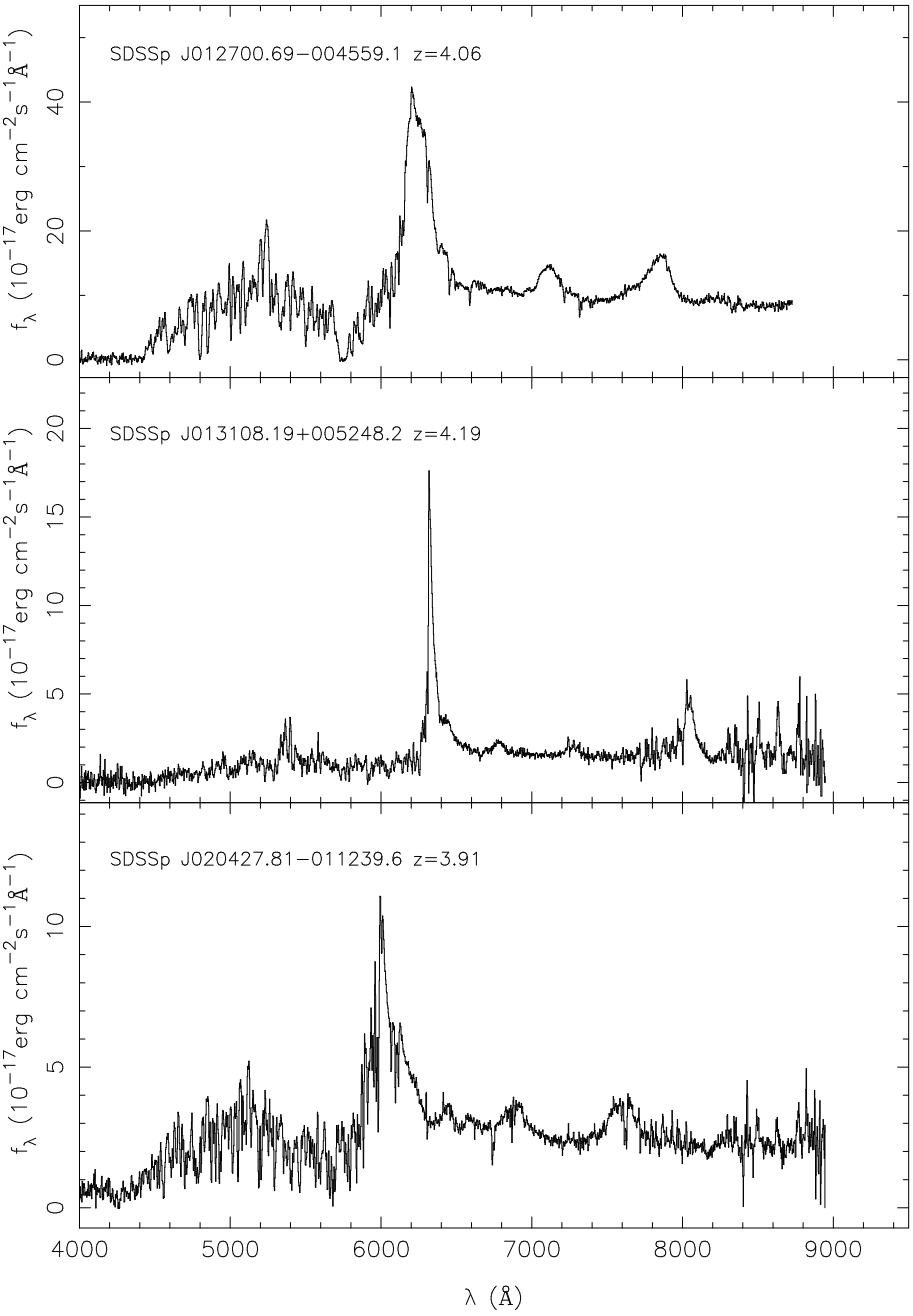

Figure 3. Continued

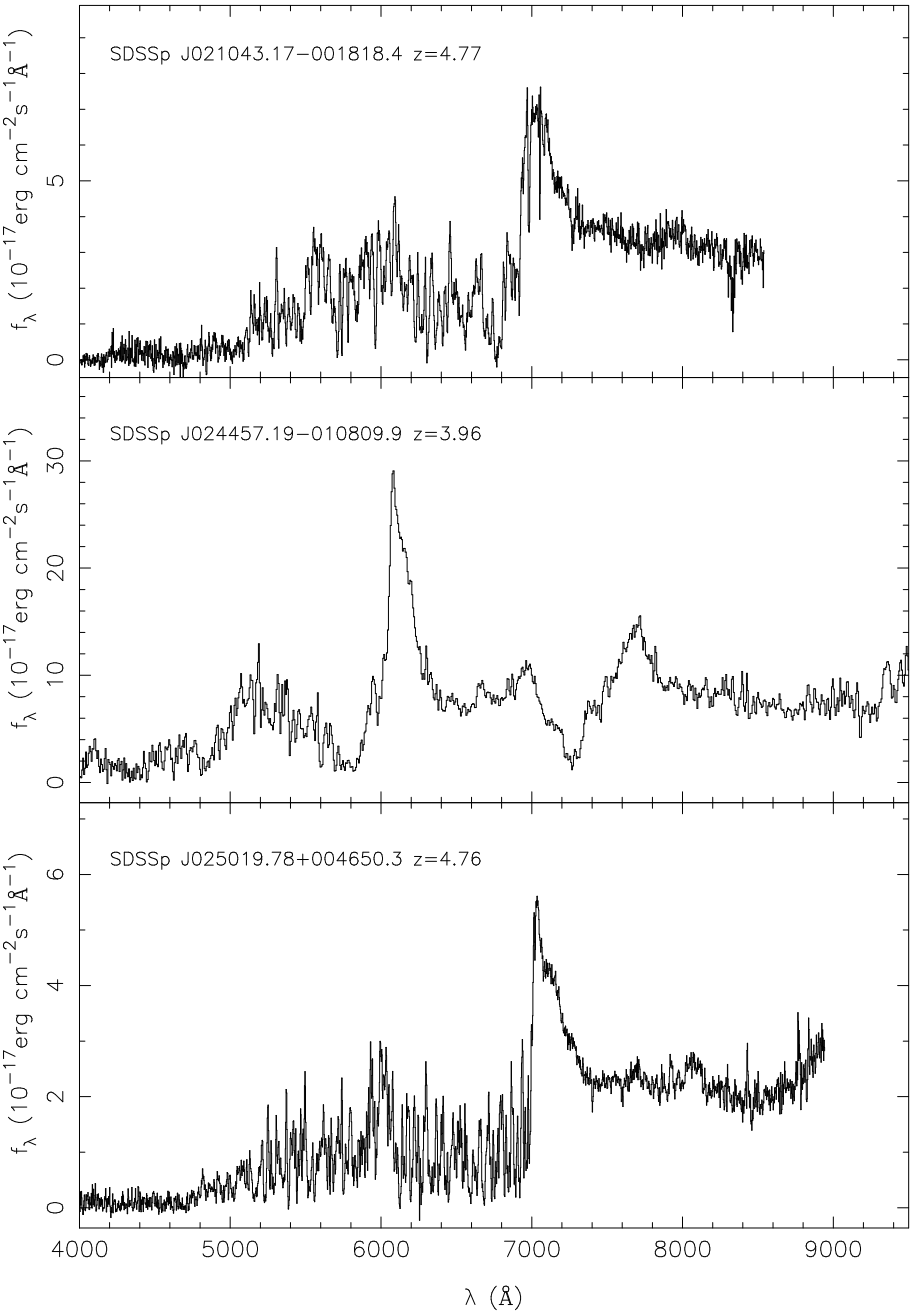

Figure 3. Continued

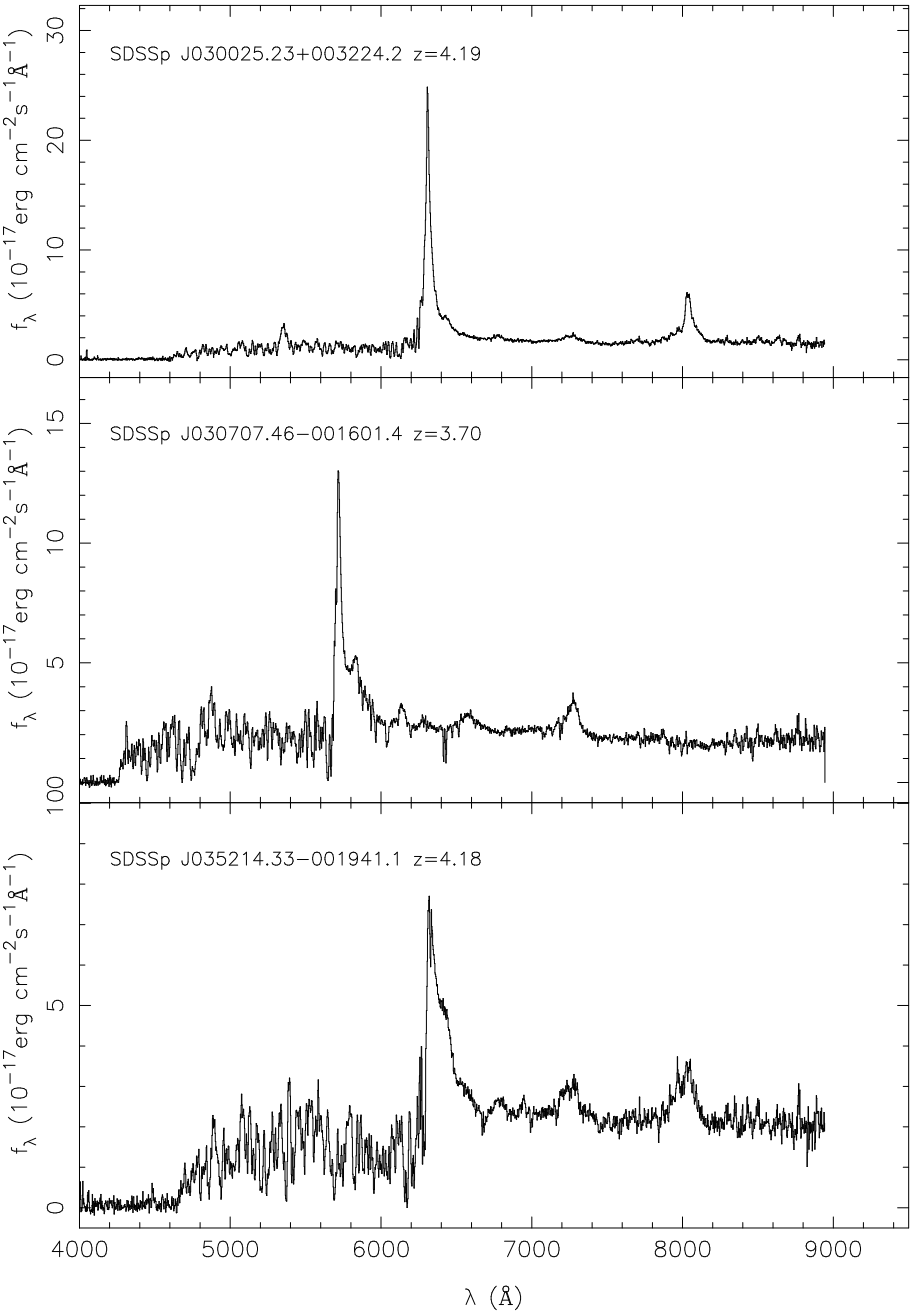

Figure 3. Continued

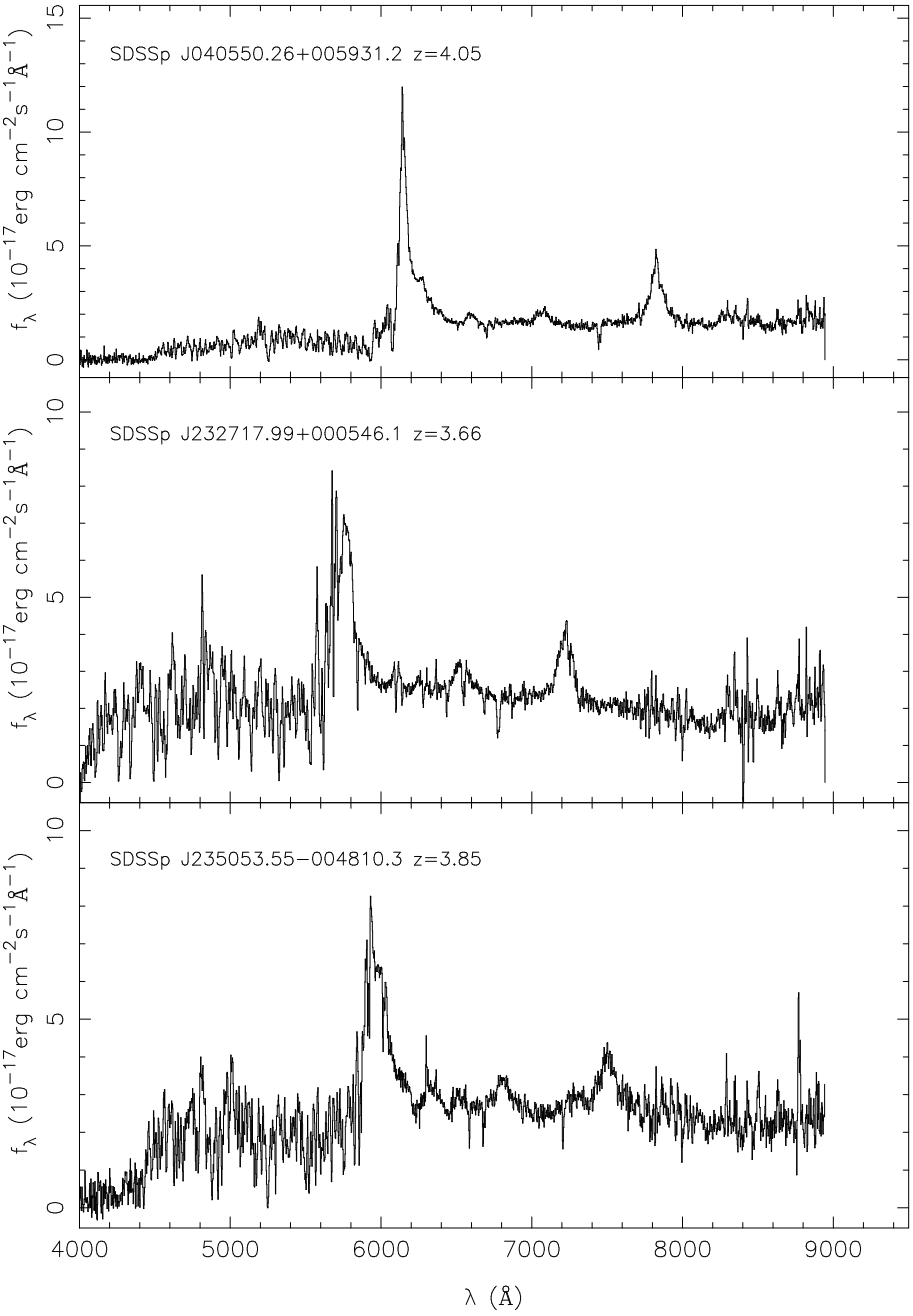

Figure 3. Continued

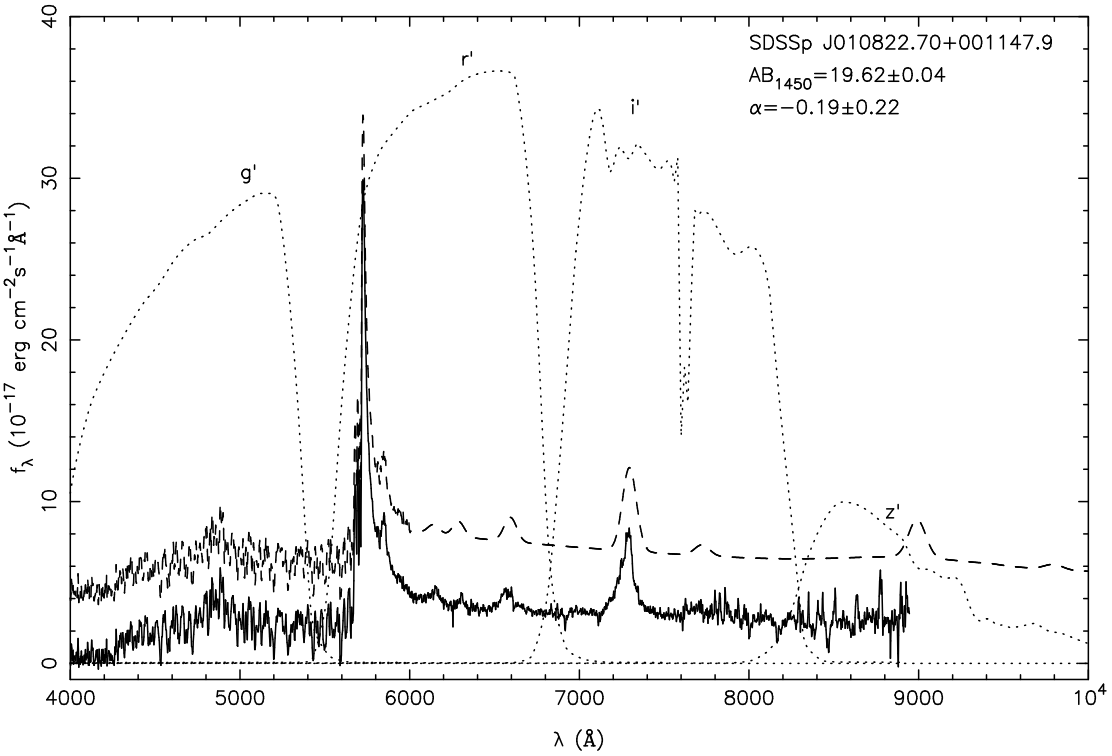

Figure 4. An illustration of the determination of the continuum properties. The solid line is the observed Keck spectrum, after applying a linear correction function to reproduce the SDSS r^* and i^* magnitudes. The dashed line is the spectral model (with an offset) that provides the smallest χ^2 for the SDSS r^*, i^* and z^* measurements. The dotted lines are the system response functions for the SDSS passbands (see Fig A-1).

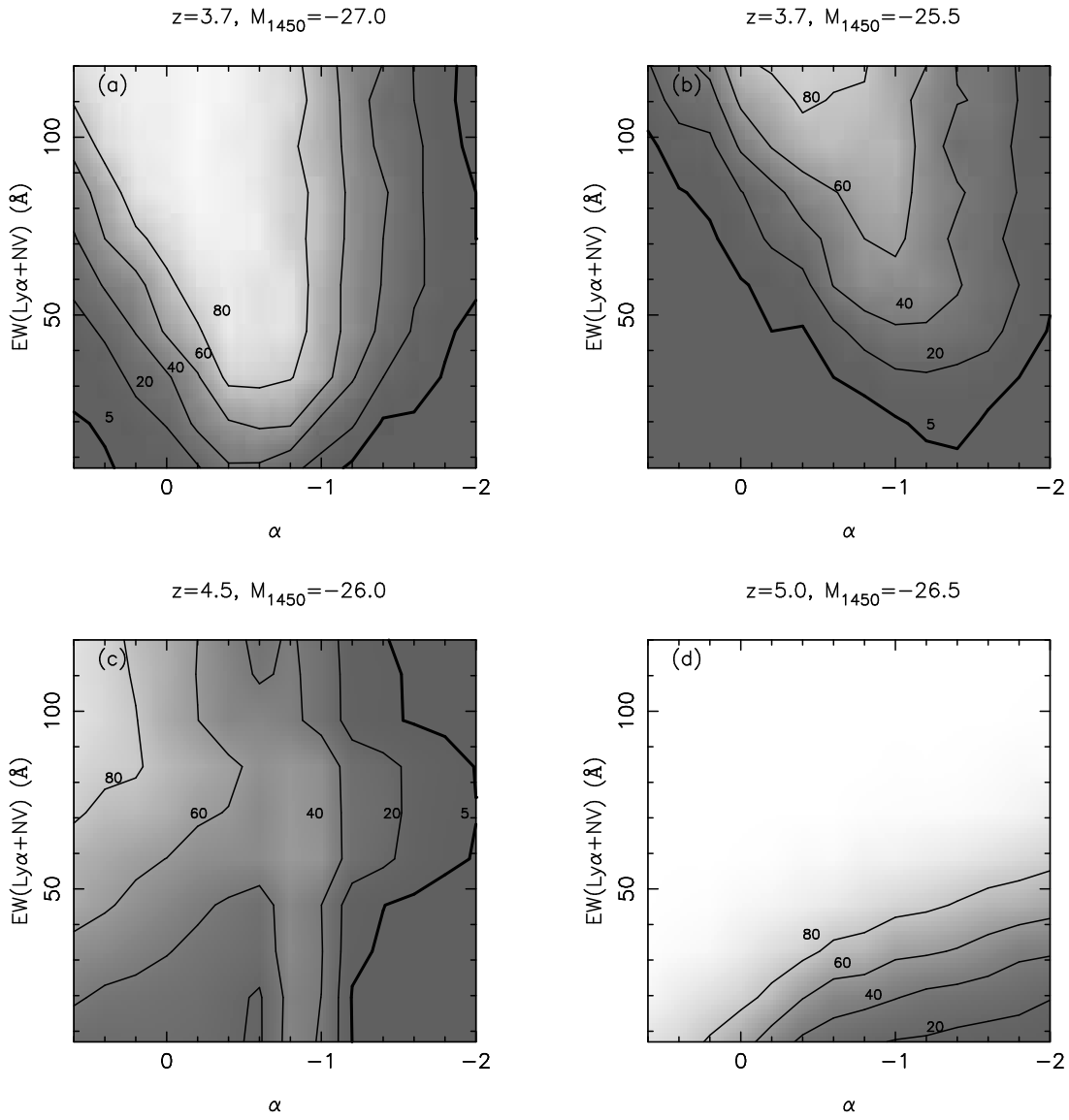

Figure 5. Quasar selection probability as a function of continuum slope and emission line strength at several different redshifts and luminosities.

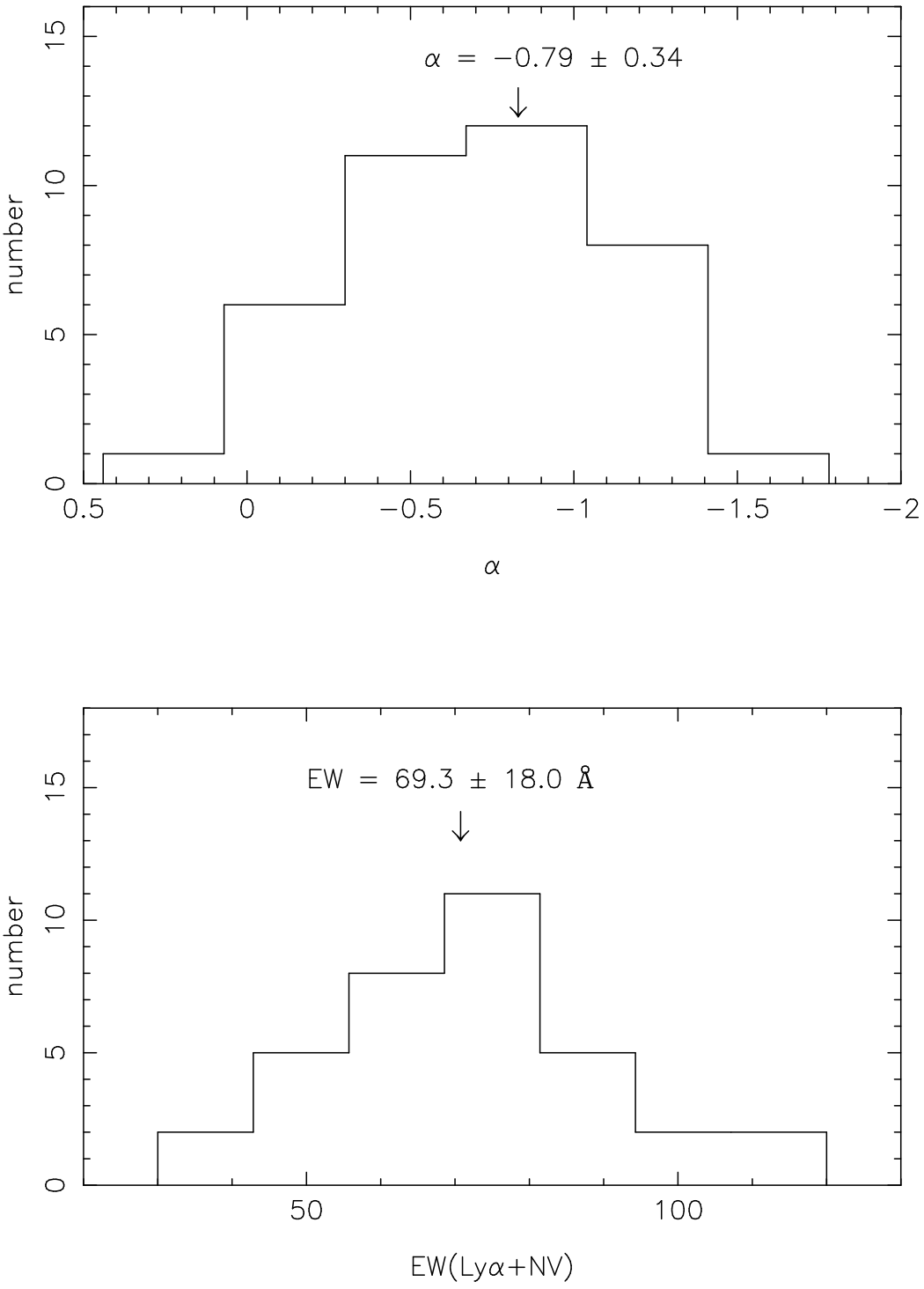

Figure 6. Distribution of the quasar continuum power-law index α (upper panel) and the rest-frame equivalent width of Lyα+NV (lower panel) for the Fall Equatorial Stripe sample. The lower panel only includes the 35 non-BAL quasars. Note that the average α from the maximum likelihood fit is not centered on the observed distribution. This is due to the fact that the selection criteria are less sensitive to objects with larger α (see Figure 5).

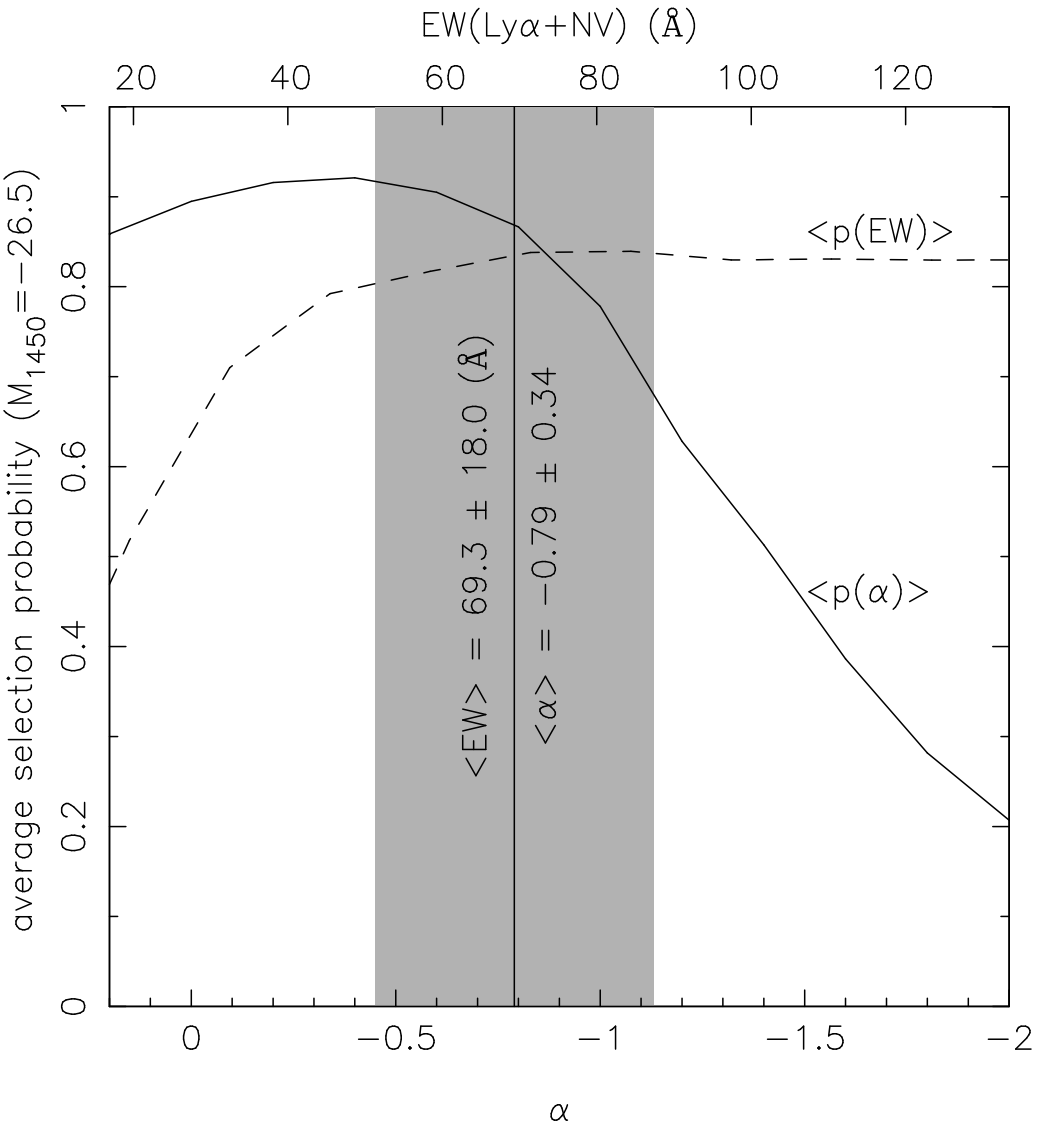

Figure 7. The average selection probability for $M_{1450} = -26.5$ and redshift range $3.6 < z < 5.0$. The solid line is the average probability as a function of continuum slope, and the dashed line is the average probability as a function of the emission line strength. The shaded area shows the $1-\sigma$ scatter of the distributions of continuum slope and emission line strength measured from the SDSS sample.

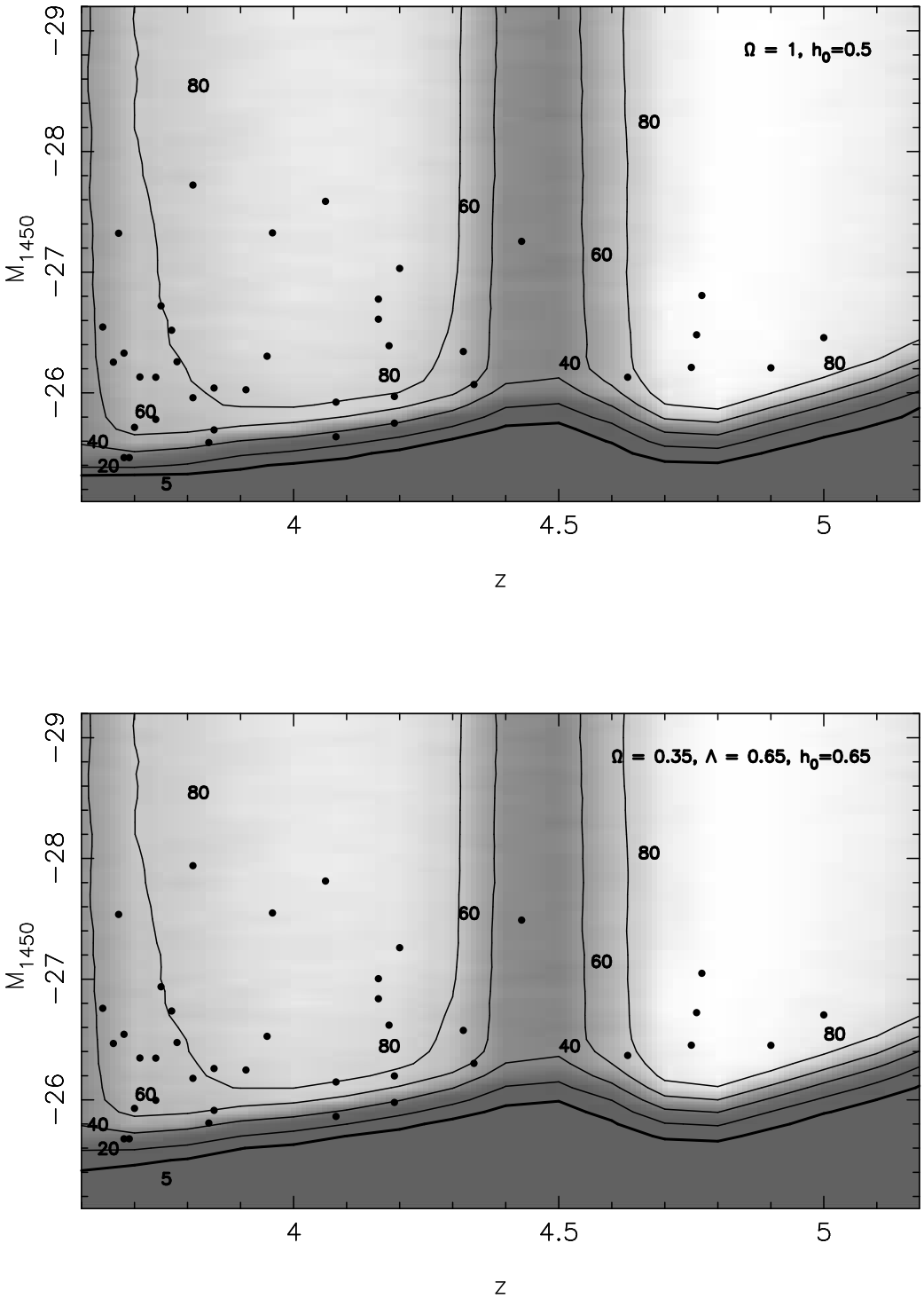

Figure 8. The selection probability of high-redshift quasars in the Fall Equatorial Stripe sample as a function of redshift and luminosity, for the $\Omega = 1$ and the Λ models. The probability contours of 5%, 20%, 40%, 60% and 80% are shown. The large dots represent the locations of the 39 quasars in the sample.

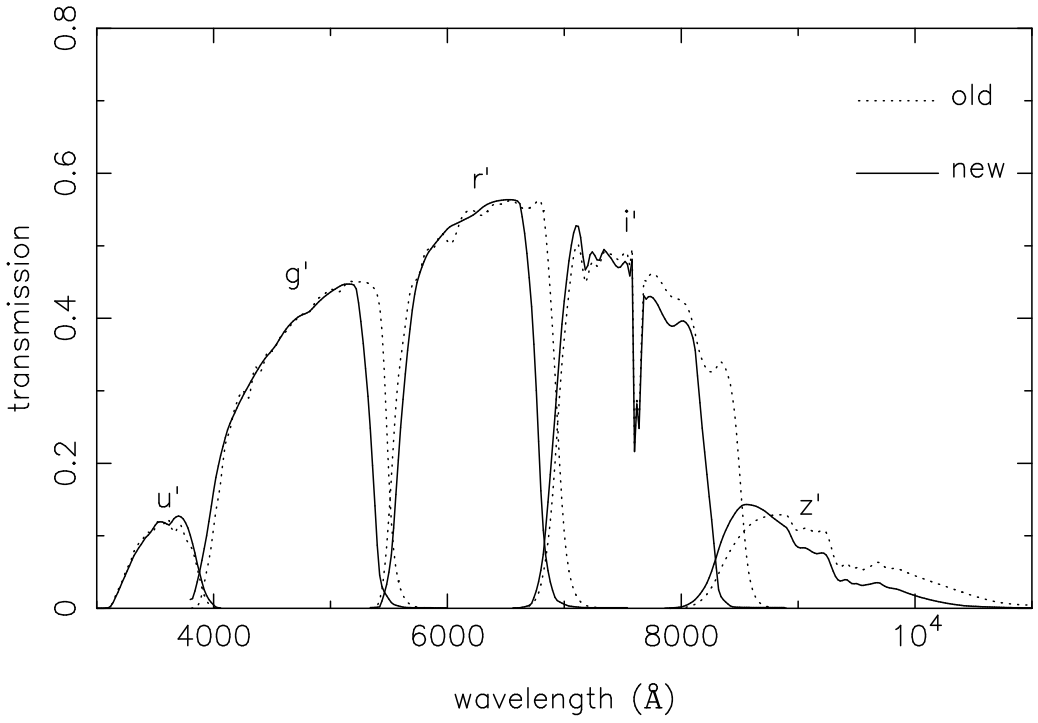

Figure A1. The SDSS photometric system response function at 1.2 airmass. The solid lines shows the new measurements in Spring 2000; the dotted lines are the old measurements before the installation of the SDSS camera in 1997. Note that the red-edge cutoffs in the g', r', i' and z' filters have moved to shorter wavelengths.

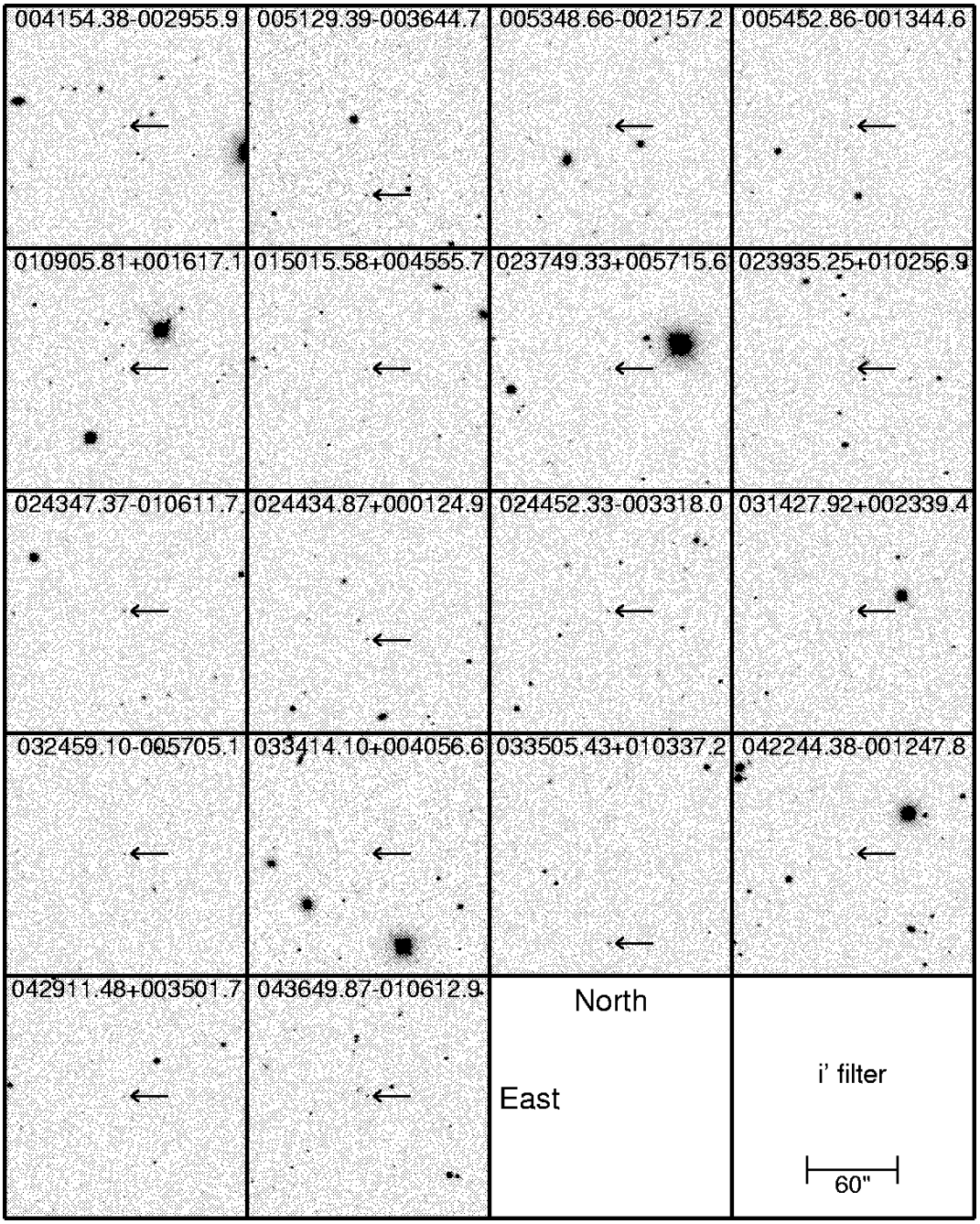

Figure B1. Finding charts for the 18 faint SDSS quasars. The data are $160'' \times 160''$ SDSS images in the i' band (54.1 sec exposure time). North is up; East is to the left.

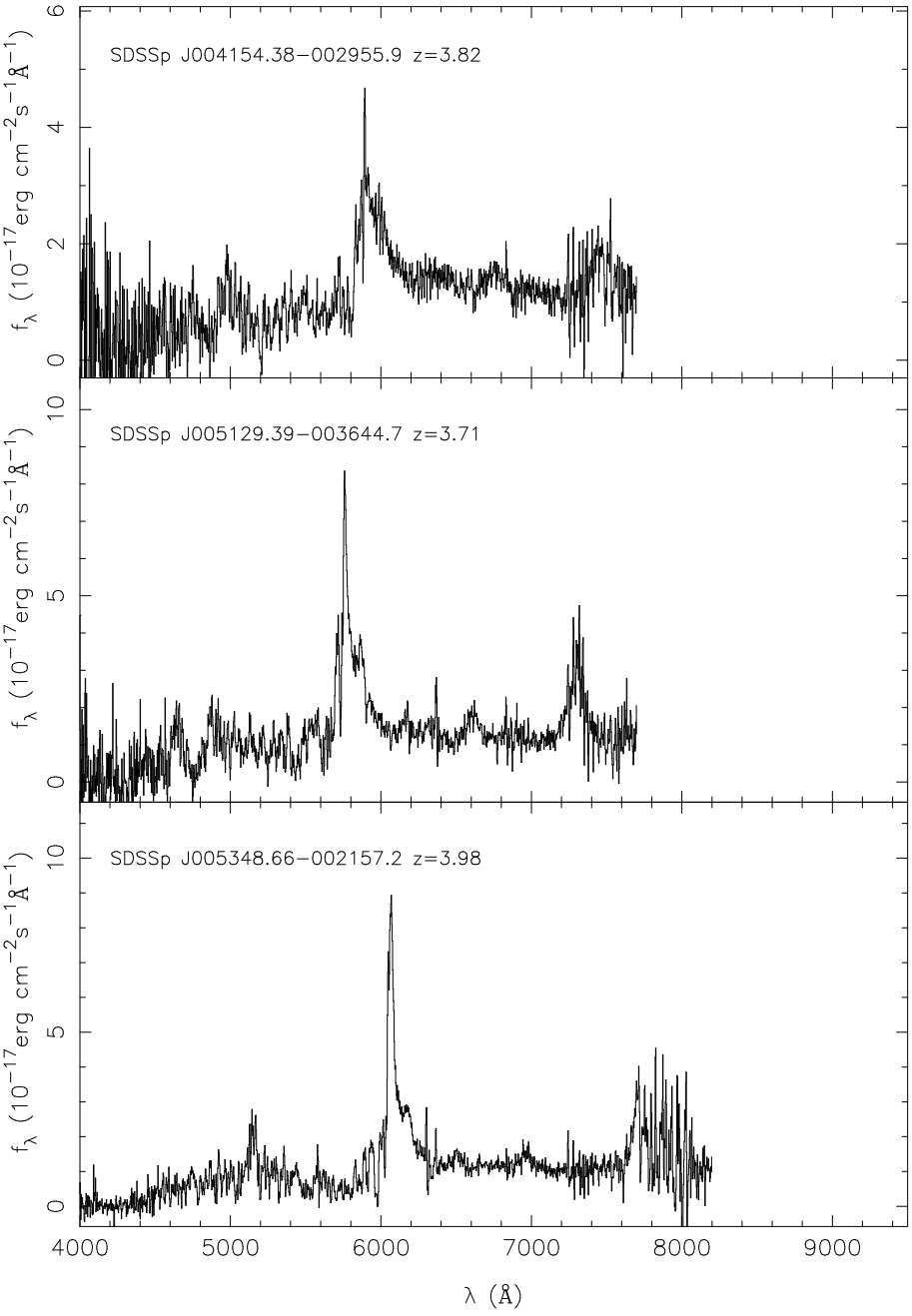

Figure B2. The spectra of 18 faint SDSS high-redshift quasars obtained with the KeckII and the ARC 3.5m telescopes (for more details, see captions of Figure 3).

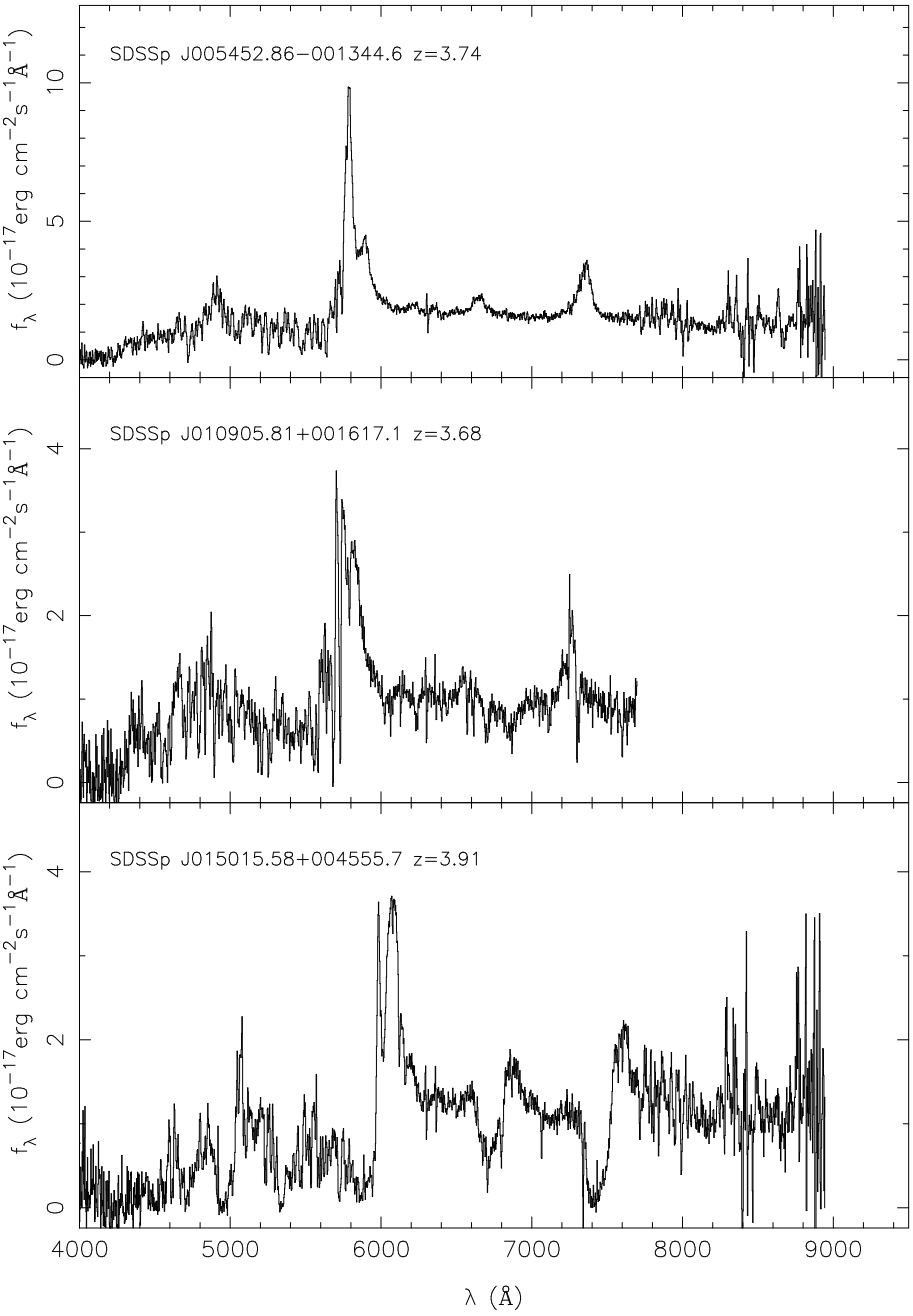

Figure B2. Continued

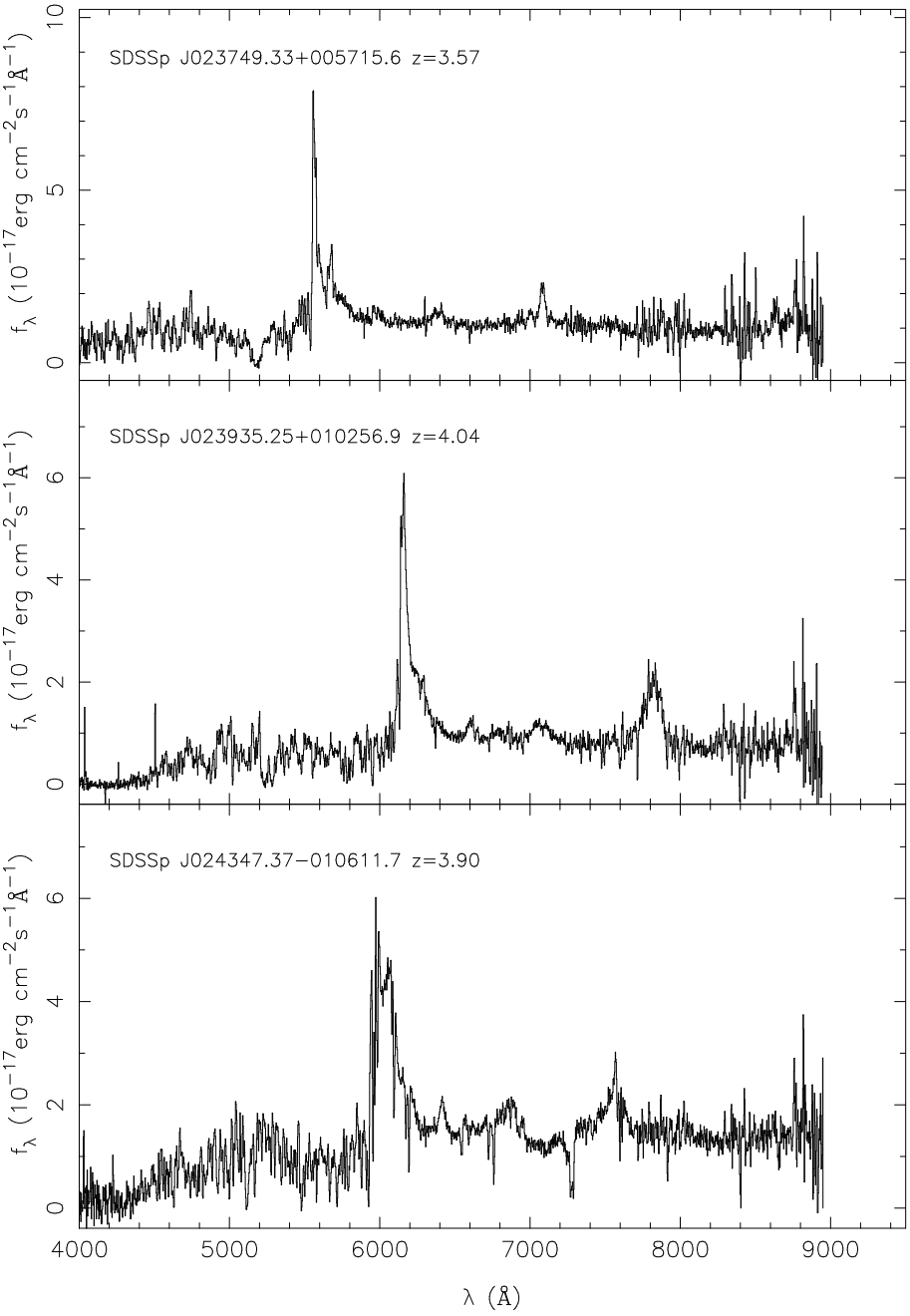

Figure B2. Continued

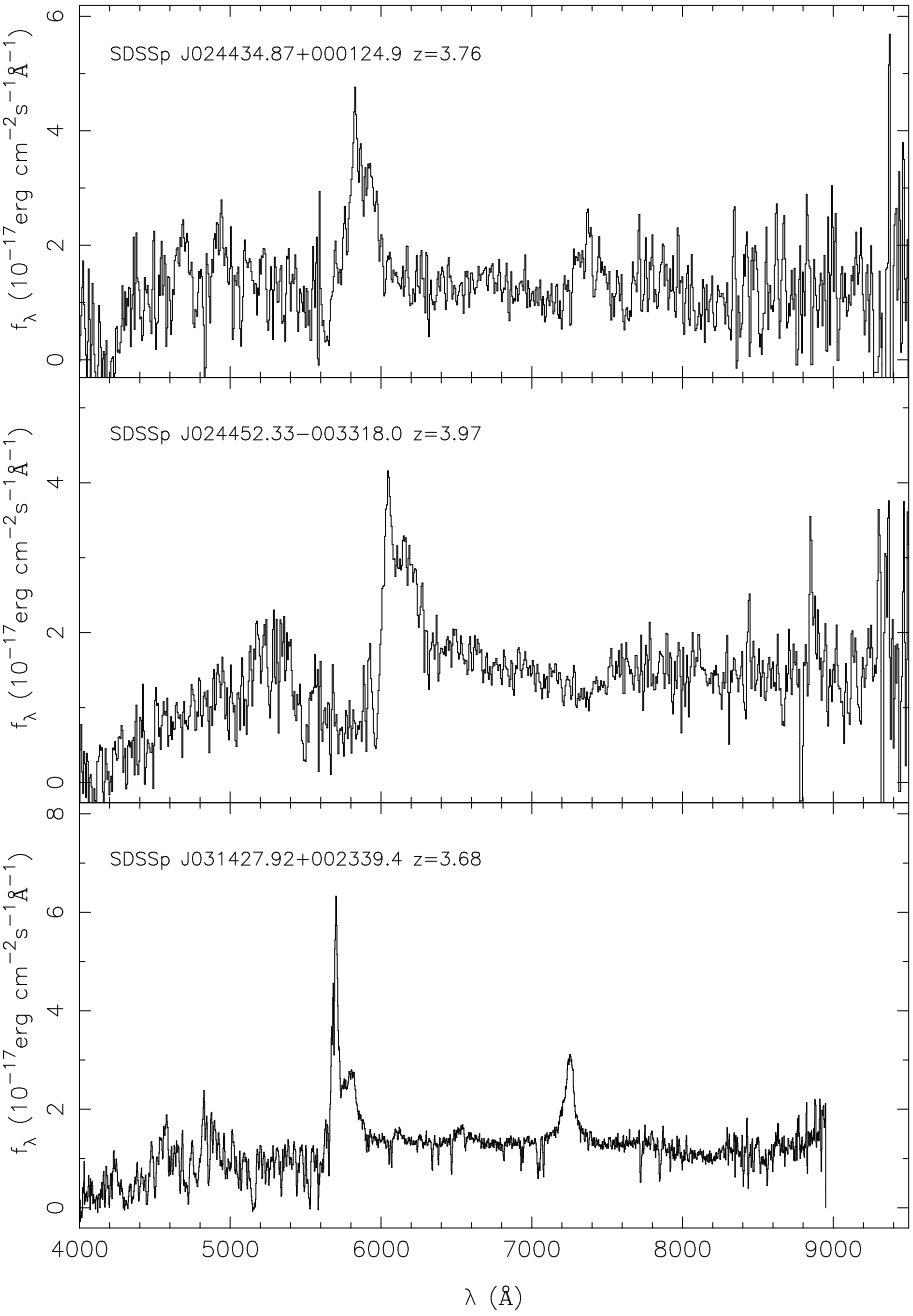

Figure B2. Continued

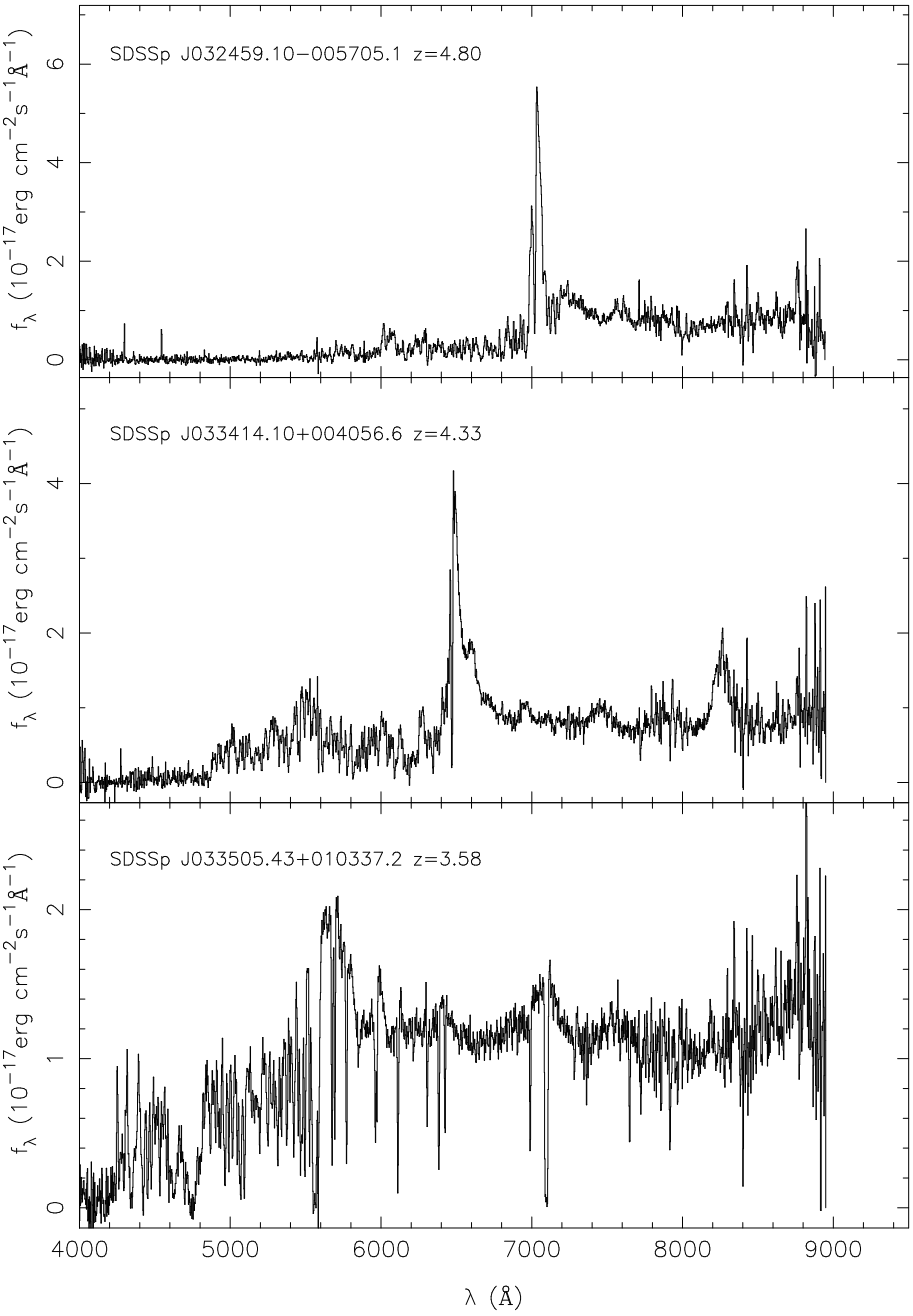

Figure B2. Continued

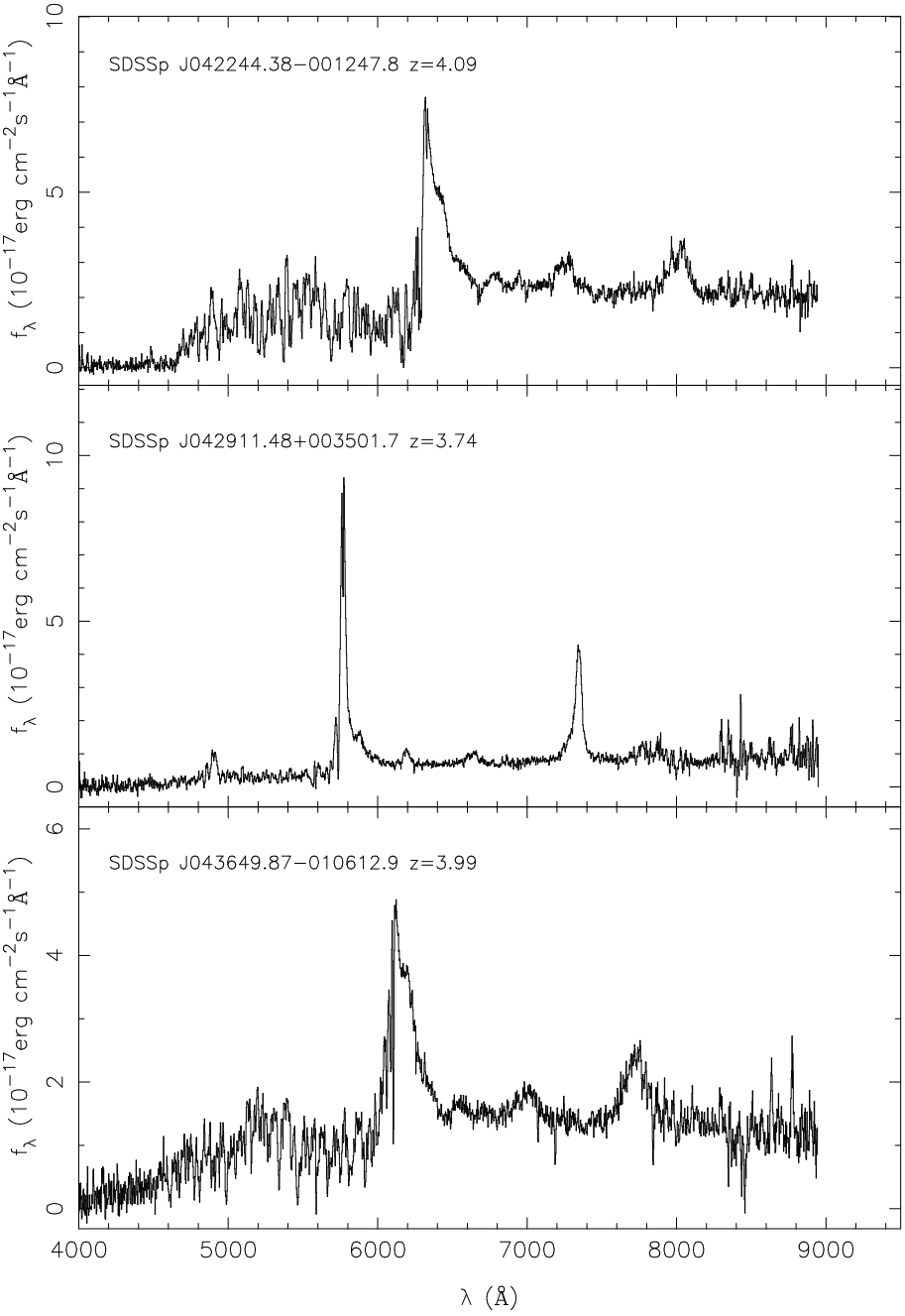

Figure B2. Continued